

RESEARCH ARTICLE

10.1029/2020MS002266

Key Points:

- Gas-phase multi-generational aging of SOA precursors is a strong source
- Loss processes such as gas-phase fragmentation pathways for SOA products need to be included for a more realistic model representation of OA
- Both strong sources and sinks are needed to explain global SOA distributions

Supporting Information:

- Supporting Information S1

Correspondence to:

M. Shrivastava,
manishkumar.shrivastava@pnnl.gov

Citation:

Lou, S., Shrivastava, M., Easter, R. C., Yang, Y., Ma, P.-L., Wang, H., et al. (2020). New SOA treatments within the Energy Exascale Earth System Model (E3SM): Strong production and sinks govern atmospheric SOA distributions and radiative forcing. *Journal of Advances in Modeling Earth Systems*, 12, e2020MS002266. <https://doi.org/10.1029/2020MS002266>

Received 28 JUL 2020


















Accepted 11 NOV 2020

Accepted article online 17 NOV 2020

©2020. The Authors.

This is an open access article under the terms of the Creative Commons Attribution License, which permits use, distribution and reproduction in any medium, provided the original work is properly cited.

New SOA Treatments Within the Energy Exascale Earth System Model (E3SM): Strong Production and Sinks Govern Atmospheric SOA Distributions and Radiative Forcing

Sijia Lou^{1,2} , Manish Shrivastava¹ , Richard C. Easter¹ , Yang Yang³ , Po-Lun Ma¹ , Hailong Wang¹ , Michael J. Cubison⁴, Pedro Campuzano-Jost⁵ , Jose L. Jimenez⁵ , Qi Zhang⁶ , Philip J. Rasch¹ , John E. Shilling¹ , Alla Zelenyuk¹ , Manvendra Dubey⁷ , Philip Cameron-Smith⁸ , Scot T. Martin⁹ , Johannes Schneider¹⁰ , and Christiane Schulz^{10,11} 

¹Pacific Northwest National Laboratory, Richland, WA, USA, ²Joint International Research Laboratory of Atmospheric and Earth System Sciences, School of Atmospheric Sciences, Jiangsu Provincial Collaborative Innovation Center of Climate Change, Nanjing University, Nanjing, China, ³Jiangsu Key Laboratory of Atmospheric Environment Monitoring and Pollution Control, Jiangsu Collaborative Innovation Center of Atmospheric Environment and Equipment Technology, School of Environmental Science and Engineering, Nanjing University of Information Science and Technology, Nanjing, China, ⁴TOFWERK, Thun, Switzerland, ⁵Cooperative Institute for Research in Environmental Sciences (CIRES) & Department of Chemistry, University of Colorado Boulder, Boulder, CO, USA, ⁶Department of Environmental Toxicology, University of California, Davis, CA, USA, ⁷Los Alamos National Laboratory, Earth Systems Observations (EES-14), Los Alamos, NM, USA, ⁸Lawrence Livermore National Laboratory, Livermore, CA, USA, ⁹John A. Paulson School of Engineering and Applied Sciences, Harvard University, Cambridge, MA, USA, ¹⁰Particle Chemistry, Biogeochemistry and Multiphase Chemistry Department, Max Planck Institute for Chemistry, Mainz, Germany, ¹¹Leibniz Institute for Tropospheric Research (TROPOS), Leipzig, Germany

Abstract Secondary organic aerosols (SOA) are large contributors to fine particle mass loading and number concentration and interact with clouds and radiation. Several processes affect the formation, chemical transformation, and removal of SOA in the atmosphere. For computational efficiency, global models use simplified SOA treatments, which often do not capture the dynamics of SOA formation. Here we test more complex SOA treatments within the global Energy Exascale Earth System Model (E3SM) to investigate how simulated SOA spatial distributions respond to some of the important but uncertain processes affecting SOA formation, removal, and lifetime. We evaluate model predictions with a suite of surface, aircraft, and satellite observations that span the globe and the full troposphere. Simulations indicate that both a strong production (achieved here by multigenerational aging of SOA precursors that includes moderate functionalization) and a strong sink of SOA (especially in the middle upper troposphere, achieved here by adding particle-phase photolysis) are needed to reproduce the vertical distribution of organic aerosol (OA) measured during several aircraft field campaigns; without this sink, the simulated middle upper tropospheric OA is too large. Our results show that variations in SOA chemistry formulations change SOA wet removal lifetime by a factor of 3 due to changes in horizontal and vertical distributions of SOA. In all the SOA chemistry formulations tested here, an efficient chemical sink, that is, particle-phase photolysis, was needed to reproduce the aircraft measurements of OA at high altitudes. Globally, SOA removal rates by photolysis are equal to the wet removal sink, and photolysis decreases SOA lifetimes from 10 to ~3 days. A recent review of multiple field studies found no increase in net OA formation over and downwind biomass burning regions, so we also tested an alternative, empirical SOA treatment that increases primary organic aerosol (POA) emissions near source region and converts POA to SOA with an aging time scale of 1 day. Although this empirical treatment performs surprisingly well in simulating OA loadings near the surface, it overestimates OA loadings in the middle and upper troposphere compared to aircraft measurements, likely due to strong convective transport to high altitudes where wet removal is weak. The default improved model formulation (multigenerational aging with moderate fragmentation and photolysis) performs much better than the empirical treatment in these regions. Differences in SOA treatments greatly affect the SOA direct radiative effect, which ranges

from -0.65 (moderate fragmentation and photolysis) to -2 W m^{-2} (moderate fragmentation without photolysis). Notably, most SOA formulations predict similar global indirect forcing of SOA calculated as the difference in cloud forcing between present-day and preindustrial simulations.

Plain language Summary Secondary organic aerosols (SOA) are formed in the atmosphere by oxidation of organic gases emitted from natural biogenic, anthropogenic, and biomass burning sources. In many regions of the atmosphere, SOA greatly contributes to fine particle mass loadings and number concentrations and affects clouds and radiation. Integrating insights from global atmospheric modeling and measurements, we show that strong chemical production achieved here by multigenerational chemistry including moderate fragmentation of SOA precursors and strong chemical sinks represented by particle-phase photolysis are needed to explain the aircraft-observed vertical profiles of SOA over multiple regions including North America, equatorial oceans, and the Southern Ocean. Photolysis reduces simulated global SOA lifetimes from 10 to 3 days. Within the same model physics and cloud treatments, we show that changes in SOA chemistry formulations change SOA wet removal lifetimes by a factor of 3. Simulations show that SOA exerts a strong direct radiative forcing in the present day ranging from -0.65 to -2 W m^{-2} . Future measurements and modeling are needed to better constrain the photolytic and heterogeneous chemical removal of SOA at high-altitude atmospheric conditions.

1. Introduction

Secondary organic aerosol (SOA) is one of the major contributors to fine particle mass and number concentrations, which impact climate (by absorbing and scattering solar radiation, influencing cloud microphysical and dynamical processes), air quality, and human health (e.g., Boffetta et al., 1997; Hu et al., 2017; Liu, Ma, et al., 2016; Ming et al., 2005; Ridley et al., 2018; Shrivastava et al., 2017; Slade et al., 2017; Tsigaridis & Kanakidou, 2018; Zhang et al., 2007, 2018). However, substantial uncertainties persist in our predictive and quantitative understanding of SOA. Global models that use simplified treatments of SOA often do not capture key features in SOA formation and evolution (e.g., Hodzic et al., 2020; Kelly et al., 2018; Myhre et al., 2009; Spracklen et al., 2011; Tsigaridis et al., 2014). Results from 34 global models included in the AEROCOM-II intercomparison depict variabilities in SOA annual chemical production by over an order of magnitude (20–120 Tg/yr), and estimates of global SOA lifetime span a wide range (2.4–14.8 days) (Heald et al., 2011; Hodzic et al., 2016; Kanakidou et al., 2005; Kelly et al., 2018; Tsigaridis et al., 2014; Shrivastava et al., 2015). Incomplete understanding of the SOA formation mechanisms, chemical transformations, and removal processes are key factors governing the large intermodel spread in simulated SOA production rate and lifetime (Shrivastava et al., 2017).

Following emission to the atmosphere, reactive organic gases undergo multigenerational aging by atmospheric oxidants, that is, OH, O₃, and NO₃ (Jimenez et al., 2009) to generate SOA. Chemical aging of semi-volatile and intermediate volatility precursors (S/IVOC) gases follows two main pathways resulting in either increased functionalization (the addition of functional groups to the carbon chain decreasing volatility and increasing SOA formation) or fragmentation (breaking of carbon-carbon bonds during oxidation forming higher volatility products (Chacon-Madrid & Donahue, 2011; Kroll et al., 2011; Lambe et al., 2012)). Once formed, SOA could also undergo accretion or oligomerization reactions in the particle phase, which reduce SOA volatility (Claeys et al., 2004; Glasius & Goldstein, 2016; Hallquist et al., 2009; Kalberer et al., 2004; Kroll & Seinfeld, 2008; Ziemann & Atkinson, 2012).

Previous modeling studies report a large sensitivity of simulated SOA to the branching ratio between functionalization and fragmentation (Glotfelty et al., 2017; Hermansson et al., 2014; Murphy et al., 2012; Shrivastava et al., 2013, 2015; Yahya et al., 2017). Using the Community Atmosphere Model Version 5 (CAM5) incorporated within the Community Earth System Model (CESM), Shrivastava et al. (2015) estimated that the global SOA production decreases from 502 to 87 Tg/yr when empirical SOA formulations turn gas-phase fragmentation on. SOA source regions are more sensitive to the branching ratio between functionalization and fragmentation compared with remote regions, given the short lifetime of most SOA precursors (approximately a few hours, Dunlea et al., 2009; Hunter et al., 2017; Shah et al., 2019). Using the CESM-NCSU model, Glotfelty et al. (2017) reported a global mean reduction ($0.03 \mu\text{g m}^{-3}$) in oxygenated organic aerosols (OOA) with significant regional decreases by up to $5.3 \mu\text{g m}^{-3}$ in South Asia, East Asia, and South Africa as the frag-

mentation branching ratio increases in their study. Previous studies using this scheme implemented in the regional Weather Research and Forecasting model with Chemistry (WRF-Chem) suggested that organic aerosol (OA) loadings in the eastern United States and central Mexico could be reduced by a factor of 2 when the fragmentation branching ratio increases 40% (Shrivastava et al., 2013; Yahya et al., 2017).

Laboratory studies also suggest that photolysis of SOA particles can remove tropospheric aerosols on time scales comparable to those of wet scavenging, and the photolysis rate depends on SOA composition, for example, differences in photolysis rates of isoprene versus terpene precursor-derived SOA and O/C ratios (Epstein et al., 2014; Henry & Donahue, 2012; Malecha et al., 2018; O'Brien & Kroll, 2019; Wong et al., 2014; Zawadowicz et al., 2020). Hodzic et al. (2016) investigated the role of photolysis on simulated SOA loadings and lifetimes in the atmosphere using a global model (GEOS-Chem). They found that SOA photolysis (with a rate equivalent to 0.04% of the NO₂ photolysis rate) reduces the global annual SOA burden from 2.31 to 0.88 Tg/yr, and overall SOA lifetime reduces from ~7 to ~3 days. In general, SOA concentrations are estimated to decrease by 20–60% in the free troposphere, and by 20–30% in the boundary layer, as a result of photolytic removal (Hodzic et al., 2015, 2016). Recently, using WRF-Chem simulations, Zawadowicz et al. (2020) showed that photolysis decreases simulated SOA concentrations by 50–66% within the boundary layer in the Amazon. Zawadowicz et al. (2020) measured a higher photolysis rate constant for SOA generated from some precursors (up to 2% of the NO₂ photolysis) as compared to the Hodzic et al. (2016) rate constant of 0.04%. However, previous studies also showed that a fraction of SOA does not photolyze (Braman et al., 2020; O'Brien & Kroll, 2019; Zawadowicz et al., 2020); for example, 20% of α -pinene and β -caryophyllene SOA, as well as 10% of isoprene SOA, were measured to be nonphotolabile in their environmental chamber measurements. In addition to wet removal and photolytic loss, recent studies suggest that the heterogeneous reactions of gas-phase oxidants (i.e., ozone and hydroxyl radical) with SOA could be additional sinks of SOA (Hu et al., 2016; Yu et al., 2019). Heald et al. (2011) suggested that heterogeneous OH oxidation could reduce global SOA burden by 15%. Hu et al. (2016) reported more than a 2-week lifetime for heterogeneous removal of isoprene epoxydiols (IEPOX)-SOA with OH radicals at ambient conditions. The relative importance of photolysis and heterogeneous reactions is expected to change latitudinally, vertically, and temporally. Additional measurements are needed to further constrain both photolytic loss and heterogeneous OH sinks of different SOA types, especially at high altitudes.

Another major uncertainty in OA arises from the aging of biomass burning organic gas- and particle-phase species (Cubison et al., 2011; Hodshire, Akherati, et al., 2019; Hodshire, Bian, et al., 2019; Jolleys et al., 2012; Shrivastava et al., 2017; Vakkari et al., 2018). Field studies frequently observe little to no net enhancement of ratio of OA to carbon monoxide (CO) in regions downwind of biomass burning sources (e.g., Akagi et al., 2012; Brito et al., 2014; Capes et al., 2008; Collier et al., 2018; Cubison et al., 2011; Forrister et al., 2015; Hodshire, Akherati, et al., 2019; Jolleys et al., 2012; Zhou et al., 2017). These observations suggest that the SOA formation in biomass burning plumes and regions downwind is limited or balanced by the loss of OA through evaporation or other mechanisms such as oxidative or photolytic chemical aging. Thus, total OA (POA + SOA) stays approximately constant at the emitted primary organic aerosol (POA) amount over biomass burning plumes. Moreover, previous modeling studies, which did not include biomass burning SOA formation processes, reported that the Global Fire Emissions Database (GFED) emissions underestimate OA concentrations by a factor of 2–4 (Kaiser et al., 2012; Reddington et al., 2016; Tosca et al., 2013). Given that OA stays approximately constant with atmospheric evolution at the emitted POA amount, this unequivocally suggests an underestimation of POA emissions in GFED. A recent study reported a near doubling of submicron particles due to SOA formation within ~3 h close to biomass burning fires (e.g., Garofalo et al., 2019; Vakkari et al., 2018). Most of these near-plume processes are subgrid scale in regional and global models; therefore, it is reasonable to effectively increase POA emissions to account for any subgrid-scale SOA formation near plumes.

Previous modeling estimates of the global aerosol-radiation interactions (RFari) from all anthropogenic aerosols range between -1.01 and -0.29 W m⁻² under clear-sky conditions based on the AeroCom phase I and II ensemble results (Myhre et al., 2013; Schulz et al., 2006), and the magnitude of RFari is dominated by anthropogenic sulfate aerosols. Large uncertainties in the contribution of anthropogenic volatile organic compounds (VOCs) to SOA formation resulted in a wide range reported for anthropogenic SOA burden (0.09 to 0.97 Tg) and an all-sky RFari ranging from -0.21 to -0.01 W m⁻². However, an observationally constrained study reported a larger RFari of OAs of -0.26 W m⁻² (Spracklen et al., 2011). These

uncertainties in SOA-induced RFari are most likely related to the poor understanding and representation of SOA processes, sources, and sinks in models (e.g., Shrivastava et al., 2017). Note that uncertainties in RFari for single aerosol species are larger than the combined uncertainty for all aerosols, likely due to compensation of errors in representing different aerosol microphysical process. Accurately speciating aerosols and their respective RFari in General Circulation Models (GCMs) and evaluating these with satellite observations is needed, according to the Fifth Assessment Report of the Intergovernmental Panel on Climate Change, AR5 IPCC (Boucher et al., 2013). Moreover, IPCC AR5 reports that uncertainties in radiative forcing due to aerosol-cloud interactions (RFaci) are even larger than for RFari, with RFaci estimates ranging from -1.8 to -0.3 W m^{-2} for total aerosols.

In this study, we compare different SOA treatments within the same global aerosol-climate model to investigate the sensitivity of SOA budgets, lifetimes, and forcing to processes governing SOA sources and sinks. We use the Energy Exascale Earth System Model (E3SMv1) to investigate (1) multigenerational oxidations of combustion-derived semivolatile and intermediate volatility SOA precursor gases (biomass burning and fossil-fuel S/IVOCs) and natural biogenic VOCs as key sources of SOA precursor gases, and (2) the photochemical removal of SOA as a sink of particle-phase SOA, which is often neglected in global SOA models. Note that both photolysis and heterogeneous reactions of SOA with OH radicals may contribute to photochemical removal of particle-phase SOA. However, we only investigate sensitivity of SOA distributions to photolytic loss in this work. A third empirical treatment includes increased POA emissions to account for missing POA emissions within GFED inventory, followed by POA aging to form hydrophilic OA at a time scale of ~ 1 day. This empirical aging scheme accounts for underestimation of biomass burning POA emissions and the observed increase in oxidation state (O:C ratio) of OA during its atmospheric aging, converting it to hydrophilic OA (Jimenez et al., 2009). The model configuration and numerical experiments are described in section 2. Section 3 presents results from the different model configurations, including differences in aerosol burden, SOA formation, and lifetime. Section 4 evaluates simulated OA from different model configurations with satellite, ground-based, and aircraft observations, and section 5 examines the impacts of SOA treatments on aerosol-radiation interaction-induced radiative effect and the radiative forcing from aerosol-cloud interactions from preindustrial (PI) to present day (PD).

2. Model Description

We use the atmospheric component of the global Earth system model E3SMv1, developed by the U.S. Department of Energy (DOE) (Rasch et al., 2019; Xie et al., 2018). E3SMv1 includes atmosphere, ocean, land surface, and sea ice components (<https://e3sm.org/model/e3sm-model-description/v1-description/v1-atmosphere/>), while the E3SM atmosphere model (EAM) is a descendant of the Community Atmosphere Model Version 5.3 (CAM5.3).

The default configuration in E3SMv1 assumes a very simple chemical mechanism with prescribed oxidants. The prescribed oxidants (OH, NO₃, and O₃) are temporally interpolated from monthly mean values, and for this study we use values appropriate for the year 2000 from Lamarque et al. (2012). We added a simple treatment of diurnal variability of oxidants: OH has a parabolic daytime profile, peaking at solar noon and is 0 at night, nitrate radicals are assumed to be 0 during daytime and constant at night, while O₃ is assumed to have a flat diurnal profile. This assumed diurnal variability of oxidants is based on our previous simulations from running gas-phase chemistry interactively in the global model (Shrivastava et al., 2015). However, predictions of SOA distributions and their impacts on radiative forcing could differ between model treatments with prescribed and interactive chemistry (Sporre et al., 2020). The modal aerosol module with four lognormal size modes (MAM4) is used, which predicts the aerosol size distribution for Aitken, accumulation, coarse, and primary carbon modes, as described by Liu, Ma, et al. (2016). A brief summary of MAM4 is provided in the next few sentences. For each mode, the size distribution is assumed to be lognormal with prescribed geometric standard deviations, and the mean dry diameter of each mode varies with changes in aerosol number and dry mass. The refractive index for each mode is calculated by Optical Properties of Aerosols and Clouds (OPAC, Hess et al., 1998) for each individual aerosol component. Aerosols are assumed to be internally mixed with other aerosol components within each mode, and Mie theory with volume mixing ratios is used to compute their optical properties (Chylek et al., 2019). Aerosol evolution in E3SM is controlled by a combination of primary particle or precursor emissions, transport (by resolved winds, turbulence,

convective clouds, and sedimentation), aerosol microphysical processes (condensation, coagulation, nucleation, and aging), cloud chemistry, dry deposition, and wet removal in MAM4 (Liu, Ma, et al., 2016). Although the hydrophobic primary carbon mode in MAM4 (compared to MAM3 that excludes a primary carbon mode) is used to treat wet removal and transport of black carbon (BC) and POA, MAM4-MAM3 differences do not affect wet removal and transport of SOA. EAMv1 also includes improved treatments compared to earlier versions of MAM for convective transport and wet removal of aerosols (that includes secondary activation), and wet removal of aerosols in stratiform clouds are described by Wang et al. (2013) and Yu et al. (2019). The resuspension treatment assumes that aerosols from evaporating raindrops are assigned to the coarse mode rather than their original mode upon complete evaporation of water (Wang et al., 2020). As discussed later, differences in SOA treatments greatly affect SOA lifetime within the model.

2.1. SOA Treatment

2.1.1. SOA Treatment in Base E3SMv1

The baseline SOA treatment in E3SMv1 is rather simple and is close to the original MAM treatment (Liu et al., 2012). It uses a single condensable organic gas species (called SOAG) and a single semivolatile SOA species in each aerosol mode, with assumed molecular weight of 150 amu and saturation vapor concentration of $0.07 \mu\text{g}/\text{m}^3$ at 288 K. The difference from earlier MAM treatments is that in E3SMv1, the condensable organic gas-phase species (SOAG) emissions are derived from the nonvolatile SOA (NVSOA) simulation of Shrivastava et al. (2015) by scaling its sources of condensable gases to the appropriate primary precursor emissions, as described in Wang et al. (2020), and the SOAG sources appear throughout the troposphere rather than at the surface. But the simple baseline treatment of E3SMv1 is not used in the present study. Here, we explicitly simulate all sources and sinks of SOA, as described below.

2.1.2. New Multigenerational SOA Treatment

In this study, we use a modified volatility basis set (VBS) approach for both SOA precursor gases and particulate SOA that includes gas-phase functionalization/fragmentation (supporting information Figure S1) and particle-phase oligomerization similar to FragNVSOA configuration of Shrivastava et al. (2015). It includes a detailed treatment of SOA precursor gas chemistry including multigenerational aging via fragmentation and functionalization reactions, particle-phase oligomerization that generates low “effective volatility” SOA, and particle-phase loss by photolysis. Photolysis of SOA was not included in Shrivastava et al. (2015) (Figure S1), but it used a different model (CESM), emissions and biogenic SOA yields, so the results from this study are not directly comparable to Shrivastava et al. (2015).

The semivolatile and intermediate volatility SOA precursor gases (S/IVOC) are emitted from biomass burning (BB), biofuel (BF), and fossil-fuel (FF) sources. The treatment of the initial oxidized SOA precursors and the choice of VBS for species from FF, BF, and BB sources are the same but different for those from biogenic (BG) sources.

2.1.2.1. Multigenerational Aging of S/IVOCs From FF, BF, and BB

As illustrated in Figure S1a, a single gas-phase IVOC species that is treated as noncondensing is coemitted with particle-phase POA, and five SVOC species with the saturation vapor concentrations (C^* at Standard Temperature and Pressure, STP) of 0.1, 1, 10, 100, and $1,000 \mu\text{g m}^{-3}$ are produced by gas-phase oxidation (Table S1). All S/IVOC species are assumed to react with OH radicals with a constant rate of $2 \times 10^{-11} \text{ cm}^3 \text{ molecule}^{-1} \text{ s}^{-1}$ (Atkinson & Arey, 2003; Robinson et al., 2007; Shrivastava et al., 2015). We track the generation number of species, defined as the number of reaction steps with the hydroxyl radical ($\text{OH}\cdot$), which produce a given VBS species, following Shrivastava et al. (2013). Since the branching ratio between fragmentation and functionalization reactions is uncertain (Murphy et al., 2012), we perform sensitivity tests investigating the response of simulated SOA to the functionalization/fragmentation branching ratio. After the first two generations of 100% functionalization, the third and subsequent generations are assumed to undergo both functionalization and fragmentation reactions determined by the respective branching ratio (FRAG). Gas-phase species in all volatility bins are available for further aging through the same functionalization and fragmentation reactions beyond Generation 3. At each oxidation step 10% of mass of each VBS species is assumed to be moved outside the VBS range (eventually forming highly volatile species like CO/CO_2 and not tracked). An assumed fraction of S/IVOCs reacting with OH (50% or 75% by mass) is assumed to fragment and consequently moved to the highest volatility bin (C^* -STP $1,000 \mu\text{g m}^{-3}$), and the remainder (40% or 15%) functionalizes and is moved to the next lower volatility bin. Functionalization is assumed to add 15% by mass from the addition of oxygen (Shrivastava

et al., 2013, 2015). Our assumed empirically determined fragmentation values of 50% or 75% follow previous studies (e.g., Shrivastava et al., 2013, 2015), due to good agreement between simulated SOA and field measurements, as documented in those studies.

2.1.2.2. Multigenerational Aging of BG SOA

The initial yields of reactions of isoprene and monoterpenes with O₃, OH, and NO₃ radicals in this study are determined from chamber measurements at low-NO_x conditions that form semivolatile products (Boyd et al., 2015; Chen et al., 2011; Kleindienst et al., 2007; Ng et al., 2007, 2008; Shilling et al., 2008; Shrivastava et al., 2019). These condensable BG semivolatile products are represented by a four-product VBS, with effective saturation vapor concentrations (C*) of 0.1, 1, 10, and 100 μg m⁻³ at 298 K and 1,013 hPa, following the yields and reaction rates in Shrivastava et al. (2019). Since BG SOA formation is represented by VBS fits to chamber data, they implicitly represent the first few generations of oxidation. Further oxidation of these BG species is assumed to cause both functionalization and fragmentation (Figure S1b).

2.1.3. Gas-Particle Partitioning

The condensation/evaporation of organic gases is calculated using a semi-implicit Euler approach with adaptive time stepping based on Zaveri et al. (2008). In this study, we also assumed semivolatile SOA “once formed” is transformed to nonabsorbing (does not participate in Raoult’s law partitioning) and nonvolatile species at the end of each model time step as described in Shrivastava et al. (2013, 2015). The transformation from semivolatile SOA to nonvolatile oligomers in the particle-phase effectively accounts for particle-phase oligomerization reactions. At the next time step gas-particle partitioning is calculated with freshly formed semivolatile species (through emissions, chemistry, or transport), but any preexisting OA from the previous time step does not enter into gas-particle partitioning calculations. As a result, only a single nonvolatile SOA species in each mode needs to be transported, after each SOA partitioning plus oligomerization calculation. We assume that for a particular C*, the semi-volatile organic compounds (SVOC) and SOA from BB/BF, FF, and BG sources behave identically (in terms of gas-phase reactions, gas-particle partitioning, and particle-phase oligomerization), so the SVOC gases and particle SOA from BB/BF, FF, and BG sources are not tracked separately in the model. This results in considerable computational savings compared to Shrivastava et al. (2015), with only eight gas species added to the default E3SM MAM4 configuration: one IVOC, five SVOCs, isoprene, and a lumped terpene. Lumped compound groups represent thousands of organic compounds within each category. Since each particle-phase chemical species is represented in three size modes, reducing the number of transported particle-phase species results in much larger computational savings than for gas-phase species.

The model does not currently include aqueous phase chemistry of isoprene epoxydiols (IEPOX-SOA), but this is a part of future planned E3SM model development efforts. IEPOX-SOA was very low during Atmospheric Tomography Mission (ATom)-2016 field campaign but contributed an average of 15% SOA over the Amazon (Hu et al., 2015).

2.1.4. Photolytic Removal of SOA

In this study, we also included photolysis as an additional sink of particle-phase SOA (for both fresh and aged SOA) with an assumed photolysis rate constant equal to 0.04% of typical NO₂ photolysis frequencies following Hodzic et al. (2016). Photolysis is an important sink of SOA especially at high altitudes where wet removal loss is low. The role of photolysis is more important for SOA (formed at all altitudes due to chemistry) compared to POA (Hodzic et al., 2020; Yu et al., 2019). Consequently, we do not include photolysis of POA in this study. As discussed later, including photolysis greatly improved model predictions with respect to in situ aircraft-based OA vertical profile measurements, especially at high altitudes (above 6 km), indicating the need for a loss pathway that affects upper atmosphere concentrations.

2.1.5. An Empirical Treatment of SOA From Combustion Sources

According to recent field studies, SOA formation from BB plumes and downwind regions is frequently balanced by the loss of OA due to evaporation (e.g., Akagi et al., 2012; Brito et al., 2014; Capes et al., 2008; Collier et al., 2018; Cubison et al., 2011; Forrister et al., 2015; Hodshire, Akherati, et al., 2019; Hodshire, Bian, et al., 2019; Jolleys et al., 2012; Zhou et al., 2017). Here, we test an empirical treatment that assumes that POA from BB (with assumed hygroscopicity parameter Kappa of 0.04, Aiken et al., 2008) is directly converted to particulate SOA (Kappa of 0.14, Brock et al., 2016) using an *e*-folding time scale of 1 day. No additional OA is added during the transport (consistent with observations), but the hygroscopicity of OA

increases due to an increase in O/C ratio (Jimenez et al., 2009). With an *e*-folding time scale of 1 day, about 60% of POA is assumed to convert to SOA after 24 h. We do not attempt to isolate BB/BF SOA from FFSOA, and the same empirical SOA treatment is used for POA emissions from all combustion sources. In this study, POA from FF contributes 21% to the total POA (sum of BB, BF, and FF) emissions, similar to van Marle et al. (2017). BG SOA is still treated using the four-product modified VBS and multigenerational chemistry as described earlier.

Previous modeling studies reported that BB emissions, particularly from GFED could be underestimated and need to be increased by factor of 2–4 to match observations (Kaiser et al., 2012; Reddington et al., 2016; Tosca et al., 2013). In this study, the BB, BF, and FF POA emissions are multiplied by a factor of 2.6, within the suggested range of those studies. The empirical treatment of SOA assumes POA is converted to SOA due to aging at a 1 day time scale equivalent to converting hydrophobic POA (low O:C ratio) to more hydrophilic and aged SOA (increased O:C) as observed in field studies (Hodshire, Akherati, et al., 2019; Jolleys et al., 2012; Shrivastava et al., 2017). The POA emissions from these sources are increased by a factor of 2.6 to account for higher OA concentrations observed close to sources as compared to GFED inventory estimates. As will be shown later, this empirical treatment of SOA shows good agreement with surface-based measurements around the globe. However, our objective is to evaluate SOA far from sources, for example, in outflow and downwind regions and at high altitudes, which requires assessing how well the model simulates the evolution, transport, and removal of SOA. OA aging time scales also vary with fuel type/plume chemistry in the real atmosphere, for example, the O:C ratio increases very fast in the rainforest fire in SW Brazilian Amazon, and in the agriculture fire in southeastern United States, but the increase in O:C ratio is highly variable (Hodshire, Akherati, et al., 2019; Hodshire, Bian, et al., 2019; Liu, Mickley, et al., 2016; Liu, Zhang, et al., 2016). The 1 day aging used here is uncertain, since effects of emissions type and combustion conditions on plume aging time scales are not considered.

2.2. Emissions

Anthropogenic and BB emissions of SO₂, BC, and POA are taken from the Community Emissions Data System (CEDS) Version 2017-05-18 data set (Hoesly et al., 2018), and the Biomass Burning emissions for the Coupled Model Intercomparison Project Phase 6 (BB4CMIP) Version 1.2 data set (van Marle et al., 2017) dataset. An organic matter to organic carbon (OM/OC) ratio of 1.4 is used to convert OC emissions to POA emissions (Aiken et al., 2008). All anthropogenic emissions used in this study are 10-year averages (from 2005 to 2014). For comparison to multiyear Moderate Resolution Imaging Spectroradiometer (MODIS) satellite aerosol optical depth (AOD), surface Aerosol Mass Spectrometer (AMS) and Interagency Monitoring of Protected Visual Environments (IMPROVE) observations, BB emissions are 10-year averages (2005–2014). However, for comparison to aircraft vertical profiles, we use year-specific SO₂, BC, POA, and S/IVOC emissions from BB with nudged meteorology. We use year-specific emissions for 2007–2008, 2013–2014, or 2015–2016 simulation periods (see next section). The BB injection heights extend up to 6 km in the middle and high latitudes (Dentener et al., 2006), while the injection height reaches 3 km altitude in tropical regions (Reddington et al., 2019). BG emissions are fixed at levels for year 2008. In this study, the monoterpene and isoprene emissions used in our model are 82 and 537 Tg/yr for PD corresponding to MEGAN1 (Guenther et al., 2006). These emissions are also consistent with recent estimates of 95 (monoterpene) and 603 Tg/yr (isoprene) from recent MEGAN-MACC (the Model of Emissions of Gases and Aerosols from Nature-Monitoring Atmospheric Composition and Climate project) data set (Sindelarova et al., 2014). For simulations with PI emissions, the 1850 emissions were used (Lathière et al., 2005).

IVOC emissions from BB, BF, and FF sources are calculated as 4 times particle-phase POA emissions, with the same spatial and temporal distribution as POA. IVOC emissions range from 0.9–9 times BB POA emissions according to measurements in both laboratory and field (e.g., Reid et al., 2005; Yokelson et al., 2013). We conducted several E3SM sensitivity simulations with multigenerational aging and high fragmentation (FRAG75) similar to the FragNVS OA scenario by Shrivastava et al. (2015), varying the IVOC emissions scale from 1.6 to 8 times POA emissions. Among all simulations, a comparison of simulated model results with observed OA concentrations and MODIS AOD indicated that the emissions scale factor of 4 was most appropriate for E3SM (Figure S2 and S3). Therefore, in this study we fix the IVOC emissions scale as a factor of 4 times POA for sensitivity simulations to evaluate the role of functionalization-fragmentation branching ratio and photolysis on simulated SOA.

Table 1
Numerical Experiments

Model ID	Emission scale from POA		Fragmentation fraction	Photolysis rate	POA convert to SOA
	NT-IVOC	POA			
FRAG75	4	1	75%	NO	NO
FRAG50	4	1	50%	NO	NO
FRAG50_PHO	4	1	50%	0.04% JNO ₂	NO
POAtoSOA	0	2.6	50%	NO	YES
FRAG75_PI	The same as FRAG75 except all emissions for preindustrial conditions.				
FRAG50_PI	The same as FRAG50 except all emissions for preindustrial conditions.				
FRAG50_PHO_PI	The same as FRAG50_PHO except all emissions for preindustrial conditions.				
POAtoSOA_PI	The same as POAtoSOA except all emissions for preindustrial conditions.				

2.3. Model Sensitivity Simulations

Simulations were performed with a prerelease version of the EAMv1, into which the new SOA treatments and the diurnally varying oxidants were implemented. Simulations were atmosphere only and used the Ne30 grid configuration that has a horizontal resolution of about 1° (5,400 spectral elements) and 72 vertical layers. Horizontal winds were nudged toward the Modern-Era Retrospective analysis for Research and Applications, Version 2 (MERRA-2) reanalysis data at a 6-h time scale (Sun et al., 2019; Zhang et al., 2014).

Sensitivity simulations were performed for (and nudged to) the periods 2007–2008, 2013–2014, and 2015 to February 2017; the first year was treated as model spin up time and discarded with the second year used for analysis. For each simulation period, a set of aircraft comparison simulations was performed. These simulations used same-year (during aircraft field campaigns) emissions of SO₂, BC, POA, and IVOC and are discussed in section 4.3. Model results were sampled daily along aircraft flight tracks. Another set of 2013–2014 simulations used 2005–2014 averaged emissions of these species. Results from these averaged-emissions simulations are discussed in sections 3, 4.1, 4.2, and 5. To estimate aerosol indirect forcing, another set of 2013–2014 simulations was performed using PI emissions (1850).

In order to quantify the impact of fragmentation reactions, photolytic loss of SOA, as well as their potential effect on climate, we perform several types of simulations (summarized in Table 1) for each of the simulation sets. In essence, functionalization causes a strong production of SOA while fragmentation and photolysis are strong SOA sinks in addition to the dry and wet removal sinks.

3. Results: Simulation of Global OA Budgets and Distributions

3.1.1. The Impacts of SOA Treatments on SOA Burden and Lifetime

Four different SOA treatments are examined for the year 2014 to investigate the impacts on SOA burden and lifetime. Simulations of the global annual mean burden and lifetime for each treatment are shown in Figure 1. The global SOA burden spans 1.7–5.0 Tg with the largest simulated burden corresponding to FRAG50 (5.0 Tg) and the smallest to FRAG50_PHO (1.7 Tg). Simulated SOA burden is sensitive to the functionalization-fragmentation branching ratio of organic gases. FRAG50, which has lower fragmentation and higher functionalization compared to FRAG75, predicts ~28% higher SOA burden than the FRAG75 configuration. With increasing functionalization (and reducing fragmentation), more S/IVOCs are moved to the lower volatility bins during aging, resulting in a stronger source of SOA. Most global models do not include continuous multigenerational aging of SOA, as considered in our study. For example, only one of the 31 global CTMs in Tsigaridis et al. (2014) used a multigenerational aging approach with VBS (but with 100% functionalization and no fragmentation) and estimated the highest global SOA loadings of 2.3 Tg.

Spracklen et al. (2011) estimated a global SOA burden of 1.84 Tg by constraining their model with AMS measurements, while Heald et al. (2010) reported a burden of 2.5 Tg C by constraining the GEOS-Chem model with satellite AOD observations. Assuming an OM/OC ratio of 2.1 (Hodzic et al., 2020) for SOA (most OA is expected to be SOA), 2.5 Tg C in their study is estimated to 5.3 Tg OA. In this study, SOA burdens calculated from all configurations approach the higher end of the previous predictions (Figure 1a), with the exception of FRAG50_PHO. Moreover, the simulated annual global SOA lifetime from the FRAG75 scenario in E3SM is greater than that estimated from the FragNVSOA scenario in CESM by Shrivastava et al. (2015) (15.5 days

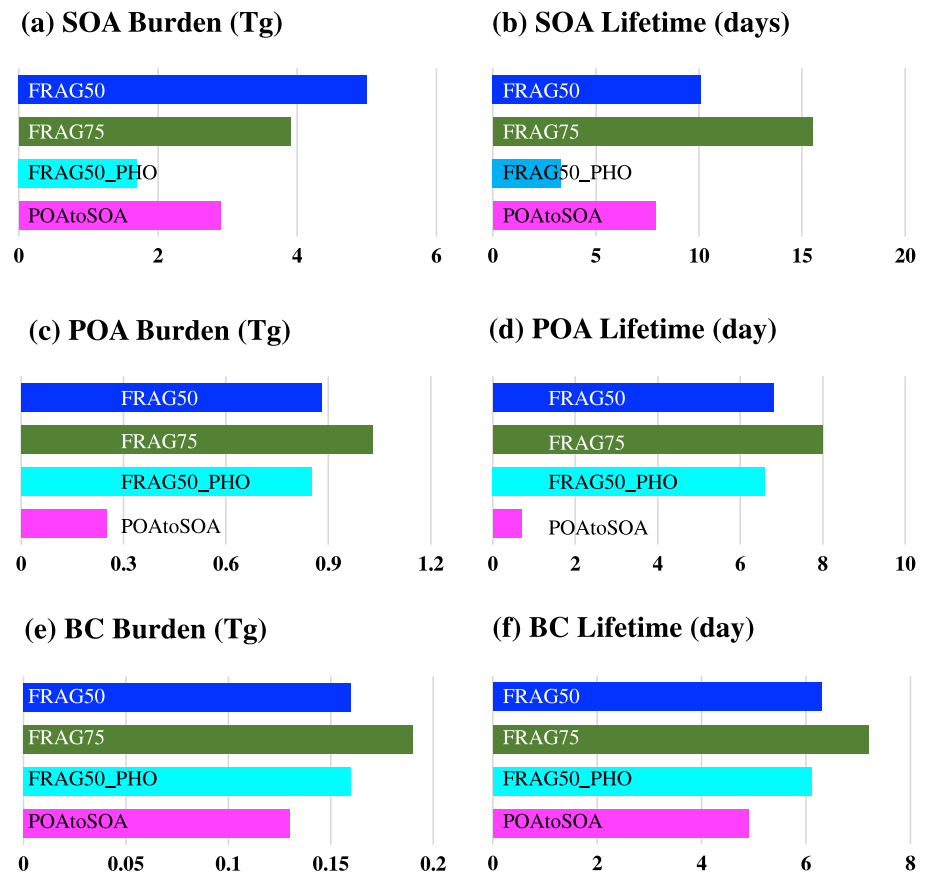


Figure 1. Annual global burden and lifetime for (a, b) SOA, (c, d) POA, and (e, f) BC from FRAG50, FRAG75, FRAG50_PHO, and POAtoSOA simulations.

in E3SM vs. 7.2 days in CESM). For similar SOA multigenerational aging treatments, key differences affecting convective transport and wet removal of aerosols between E3SM and CESM likely govern the factor of 2 longer SOA lifetime in E3SM compared to CESM (Rasch et al., 2019).

3.1.2. Combined Effects of Wet Removal and Gas-Phase Fragmentation Without Photolysis

Particles are more efficiently removed by wet deposition compared to volatile gases. With higher fragmentation, more S/IVOC precursor gases move to the highest volatility bin and are transported as gases to the upper troposphere, where losses due to wet deposition are minimal. Subsequently, due to cold temperatures in the upper troposphere, these S/IVOCs condense to form SOA. This results in longer atmospheric lifetime for SOA, that is, 15.5 versus 10.1 days in FRAG75 and FRAG50, respectively. Near-source regions and closer to the surface, FRAG75 results in greater fraction of S/IVOC to be in the gas-phase due to higher fragmentation compared to FRAG50. These S/IVOC gases are then transported to the upper troposphere where they condense, increasing SOA formation. Note that most laboratory measurements are not conducted at chemical and meteorological conditions representing high altitudes, therefore SOA parameterizations derived from those measurements would lead to a model bias for S/IVOCs condensation and SOA lifetime.

The POAtoSOA simulation with the empirical treatment of SOA predicts much smaller SOA burden and lifetime compared to the simulations with VBS formulations and multigenerational chemistry. POAtoSOA simulated 2.9 Tg SOA burden and 7.9 days SOA lifetime are in better agreement with previous studies (Hodzic et al., 2016; Spracklen et al., 2011; Tsigaridis et al., 2014). This simulation has faster SOA formation at a ~1-day time scale, and bypasses slower gas-phase multigenerational chemistry. However, as discussed later, the empirical POAtoSOA treatment overpredicts OA at high altitudes compared to some recent aircraft field observations, since it does not include SOA photolysis. Moreover, the empirical POAtoSOA configuration largely underestimates POA burden and lifetime.

Table 2
Summary of Budget for SOA, POA, and BC

	FRAG75	FRAG50	FRAG50_PHO	POAtoSOA
SOA BURDEN (Tg)	3.9	5.0	1.7	2.9
SOA EMIS (Tg)	92.0	180.6	181.9	135.7
SOA DRYDEP (Tg/yr)	13.5	27.0	14.5	24.3
SOA WETDEP (Tg/yr, STRA+CONV)	78.4	153.2	77.6	111.1
SOA WETDEP STRATIFORM (Tg/yr)	42.5	69.1	38.2	43.4
SOA WETDEP CONVECTIVE (Tg/yr)	36.0	84.1	39.4	67.7
SOA Photolysis (Tg/yr)			89.3	
SOA Lifetime (days)	15.5	10.1	3.4	7.9
POA BURDEN (Tg)	1.03	0.88	0.85	0.25
POA EMIS (Tg)	47.1	47.1	47.1	122.4
POA DRYDEP (Tg/yr)	16.5	15.6	15.6	21.0
POA WETDEP (Tg/yr, STRA+CONV)	30.4	31.3	31.3	11.6
POA WETDEP STRATIFORM	13.1	12.9	12.7	4.0
POA WETDEP CONVECTIVE	17.3	18.4	18.6	7.6
POA Lifetime (days)	8.0	6.8	6.6	0.7
BC BURDEN (Tg)	0.19	0.16	0.16	0.13
BC EMIS (Tg)	9.4	9.4	9.4	9.4
BC DRYDEP (Tg/yr)	3.7	3.6	3.6	3.4
BC WETDEP (Tg/yr, STRA+CONV)	5.6	5.8	5.8	5.9
BC WETDEP STRATIFORM	2.6	2.6	2.5	2.4
BC WETDEP CONVECTIVE	3.0	3.2	3.2	3.5
BC Lifetime (days)	7.3	6.3	6.1	4.9

3.1.3. Role of Photochemical Loss on SOA Burdens and Lifetimes

The relative importance of photolysis and heterogeneous reactions is expected to change horizontally, vertically and temporally. For example, at higher altitudes, OH concentrations (in molecules cm^{-3}) decrease compared to near-surface concentrations, as air density decreases (Figure S4 in supporting information), while the colder temperatures also reduce the rate of OH oxidation. In contrast, solar radiation is substantially higher in the upper troposphere due to less cloud coverage. Consequently, relative importance of photolysis compared to heterogeneous chemistry likely increases with altitude. Hodzic et al. (2015, 2016) suggest that photolytic loss is a major sink for SOA in the atmosphere, comparable to the wet removal sink. Similarly, our FRAG50_PHO simulations predict that photolysis and wet scavenging result in similar SOA loss rates (49% and 43%, respectively Table 2).

In contrast, when photolytic loss of SOA is not included in our three other model configurations, wet scavenging is estimated to be the dominant sink, that is, 82–85% of SOA is removed from the atmosphere via wet scavenging with no loss due to photolysis. Net annual SOA production and removal (sum of photolysis and wet deposition) rates are similar between FRAG50 and FRAG50_PHO; however, the efficient removal of SOA from the atmosphere by photolysis results in a significant decrease in the global SOA burden by a factor of ~3. Global lifetime of SOA decreases from 10 days (mainly due to wet removal) in FRAG50 to 3 days (photolysis and wet removal) in FRAG50_PHO indicating that photolysis is a stronger sink of SOA compared to wet removal over short time scales (approximately days). It is likely that there could be compensating errors in SOA-related to stronger photolysis and weaker wet deposition in E3SM. Laboratory measurements by Zawadowicz et al. (2020) suggest that isoprene and monoterpene SOA decays at the rate of 1.5% and 0.8% of JNO_2 , respectively, which are higher than the 0.04% of JNO_2 values used in this study and previous studies (Hodzic et al., 2016; Malecha et al., 2018). However, Zawadowicz et al. (2020) also reported that 10% and 30% of isoprene and monoterpene SOA, respectively, did not undergo photolytic loss, which should be taken into account in future studies.

FRAG50_PHO predicts a similar global SOA burden and lifetime in E3SMv1 as a recent study using CESM Version 2 (CESM2, Tilmes et al., 2019). While both E3SMv1 and CESM2 include photolytic loss of SOA, the VBS treatment in these models differs in several aspects. For example, our E3SMv1 study includes treatment of multigenerational chemistry including fragmentation and functionalization with prescribed diurnally varying oxidants. While CESM2 uses fixed effective SOA yields, ozone and oxidants are prescribed in CESM2 (Tilmes et al., 2019).

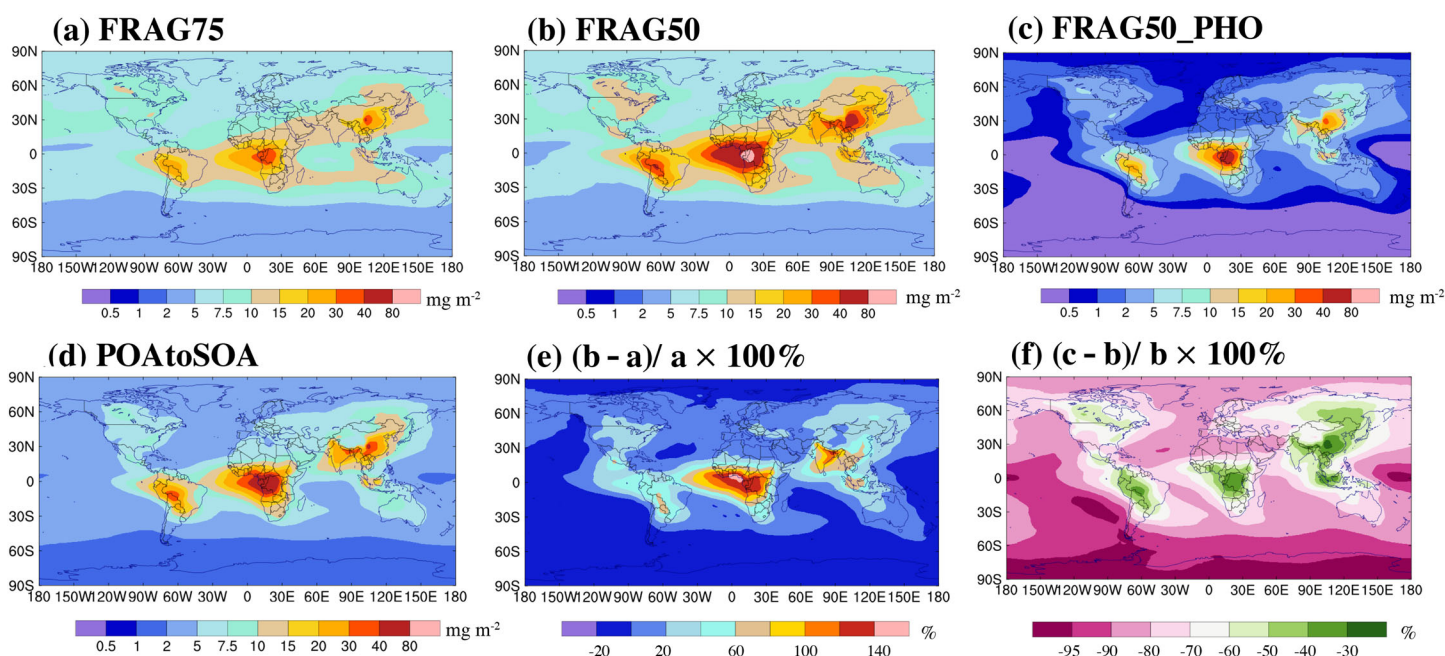


Figure 2. The annual global SOA burden (mg m^{-2}) for (a) FRAG75 (75% fragmentation), (b) FRAG50 (50% fragmentation), (c) FRAG50_PHO (50% fragmentation and SOA photolysis), (d) POAtoSOA (the empirical SOA treatment), (e) the relative differences between (b) and (a) $((\text{FRAG50} - \text{FRAG75}) / \text{FRAG75} \times 100\%)$, and (f) the relative differences between (c) and (b) $((\text{FRAG50_PHO} - \text{FRAG50}) / \text{FRAG50} \times 100\%)$.

3.2. Simulated Global SOA Distributions

3.2.1. The Impact of Functionalization/Fragmentation on SOA

The simulated annual mean column burden of SOA, which includes the sum of SOA in the Aitken, accumulation, and coarse modes for FRAG75, is shown in Figure 2a. SOA burden peaks in BB regions such as Central Africa (and in downwind regions over the Atlantic Ocean), South America, and the boreal forest regions of Canada, with values in the range of $10\text{--}40 \text{ mg m}^{-2}$. BB S/IVOC precursors contribute more than 50% to the global total S/IVOC emissions from all precursors. Simulated SOA burden also exhibits a maximum value (up to 40 mg m^{-2}) in East Asia, mainly due to BF and FF emissions in the industrial regions of East Asia. The simulated magnitude and spatial distribution of SOA column burdens are consistent with previous global modeling studies (Hodzic et al., 2016; Shrivastava et al., 2015).

Figures 2b and 2e show the simulated annual mean SOA column burden for FRAG50, along with the relative difference between FRAG50 and FRAG75 $((\text{FRAG50} - \text{FRAG75}) / \text{FRAG75} \times 100\%)$, respectively. Decreasing fragmentation with an increase in functionalization reactions results in a stronger source of SOA. Thus, over major BB regions, for example, South America, Africa and their downwind regions, SOA burdens increase by 140%, with a decrease in fragmentation fraction from 75% to 50%. Over other BB source regions in North America, Europe, and Russia, the simulated SOA burden from FRAG50 increases by 20–60% compare to FRAG75. While FRAG50 predicts higher SOA burdens near-source regions compared to FRAG75, the SOA burden exhibits a different trend in the Arctic and over most ocean regions in the Southern Hemisphere. In these remote regions, FRAG50 predicts a decrease in SOA burden by 10–20% compared to FRAG75. Because FRAG50 is associated with increased particulate SOA matter near-source regions, long-range transport and subsequent particle aging, which is linked to more efficient wet removal, indicates a stronger sink for SOA in FRAG50 compared to FRAG75. Increased fragmentation under FRAG75 results in more gas-phase S/IVOC precursors compared to FRAG50 that can be transported to remote locations, and these precursors may contribute to additional SOA formation.

In order to better understand how SOA formation changes during transport and with the branching ratio between fragmentation and functionalization, especially at high altitudes, Figures 3a and 3b shows the annual and zonal mean vertical distribution of SOA corresponding to the two model configurations. Both the FRAG75 and FRAG50 configurations simulate SOA peaks over tropical regions between 30°S and 40°

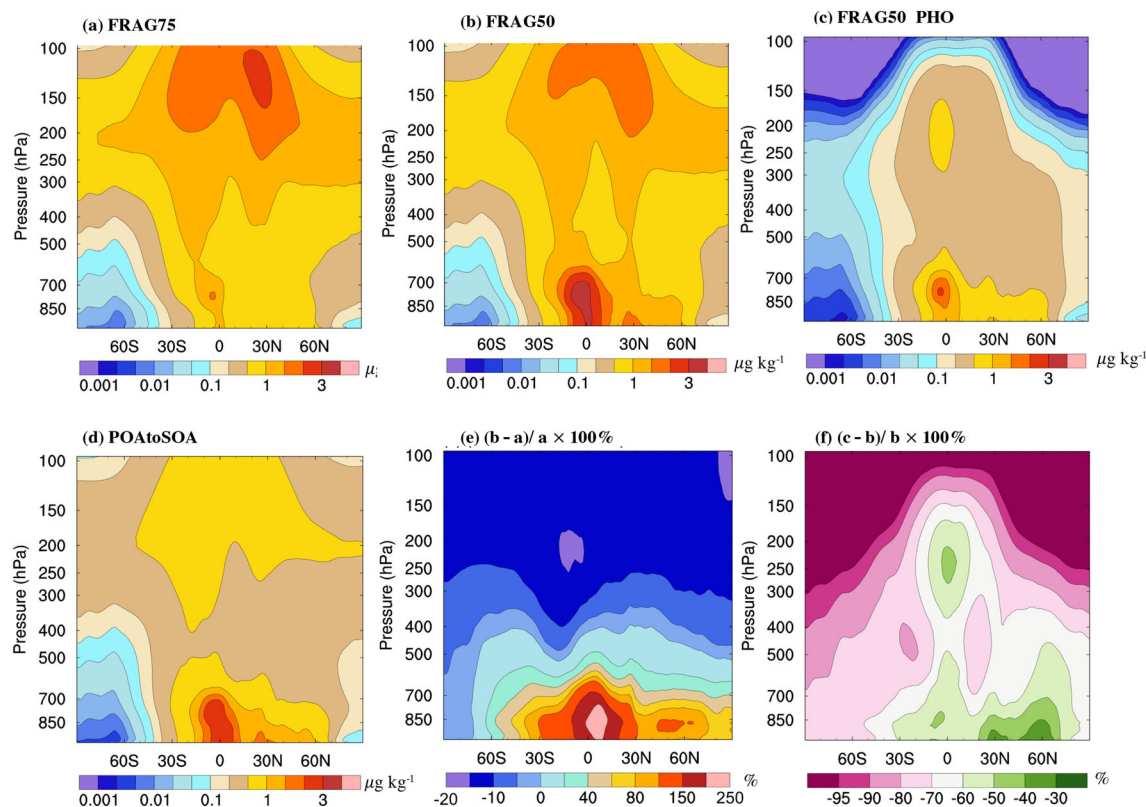


Figure 3. Annual and zonal mean distributions of SOA mixing ratios ($\mu\text{g kg}^{-1}$) for (a) FRAG75 (75% fragmentation), (b) FRAG50 (50% fragmentation), (c) FRAG50_PHO (50% fragmentation and SOA photolysis), (d) POAtSOA (the empirical SOA treatment), (e) the relative differences between (b) and (a) $((\text{FRAG50} - \text{FRAG75})/\text{FRAG75} \times 100\%)$, and (f) the relative differences between (c) and (b) $((\text{FRAG50_PHO} - \text{FRAG50})/\text{FRAG50} \times 100\%)$.

N, but at different altitudes. The FRAG50 configuration simulates high concentrations of SOA in both the lower troposphere (surface to 600 hPa [up to $5 \mu\text{g kg}^{-1}$]) and in the upper troposphere above 200 hPa (up to $2 \mu\text{g kg}^{-1}$ in Figure 3b). In contrast, FRAG75 simulates the largest SOA concentrations in the upper troposphere ($1.5\text{--}3 \mu\text{g kg}^{-1}$ in Figure 3a).

The relative differences between the two functionalization/fragmentation configurations are shown in Figure 3e. With decreasing fragmentation, SOA concentrations are estimated to increase by up to 250%, corresponding to regions of BB emissions and their typical injection height (~ 3 km) in the lower troposphere. However, at higher altitudes, FRAG50 predicts lower SOA mixing ratios than FRAG75. Gas-phase organics are removed less efficiently than particles via wet scavenging. These semivolatile organics can subsequently be transported to higher altitudes where lower temperatures are conducive to condensation and hence SOA formation.

Similar to effects on the SOA burden, the branching ratio between fragmentation and functionalization changes simulated cloud condensation nuclei (CCN diagnosed at supersaturation 0.1%) concentrations (Figures S5 and S6 in supporting information), especially in BB regions of South Africa, South America, and North America. Overall FRAG50 predicts higher global CCN burdens compared to FRAG75 globally with stronger increases (up to 120%) in BB regions of South Africa and South America (Figure S5e). Vertically, FRAG50 increases CCN mixing ratios by 40–70% below 500 hPa in the lower troposphere but predicts lower CCN than FRAG75 by 10% above ~ 6 km (Figure S6e). Our study demonstrates that the ratio of gas-phase fragmentation to functionalization is a key parameter that impacts the vertical distribution and long-range transport of SOA and also strongly impacts CCN concentrations.

3.2.2. Impacts of Photolysis

In order to understand the impact of in-particle photolysis reactions on SOA concentrations, we compare results with SOA photolysis turned on/off (FRAG50_PHO and FRAG50, respectively). The relative difference in annual mean SOA column burden between FRAG50_PHO and FRAG50 $((\text{FRAG50_PHO} - \text{FRAG50})/$

FRAG50 \times 100%) is shown in Figure 2f. Photolysis reduces SOA globally with stronger reductions over remote regions compared to near-source regions, due to the increased available aging time during OA transport for this process, which acts on time scales of several hours to days. Thus, photolysis decreases simulated peaks of SOA ($>20 \text{ mg m}^{-2}$) located downwind of BB/industrial source regions over Central Africa, South America, and China by 20–50%. Over remote regions, the reductions in SOA concentrations are even larger, with decreases exceeding 80%. Our results are consistent with Hodzic et al. (2016, 2020) who predicted an 80% reduction in SOA over remote regions, and a 10–30% reduction near-source regions where the photolytic loss pathway plays an important role that is comparable to wet deposition.

Figures 3b and 3c show the simulated annual zonal mean vertical distributions of SOA concentrations for FRAG50 and FRAG50_PHO, respectively. Compared to FRAG50, SOA photolysis significantly reduces SOA concentrations in the whole troposphere, especially in the free troposphere and over remote regions (Figure 3f). Photolysis reduces SOA concentrations by 30–60% in the boundary layer over major source and corresponding outflow regions, and by 50–90% in the middle and upper troposphere. Consistently, photolysis decreases CCN concentrations (Figure S6f) over remote regions and high altitudes (above 400 hPa) by \sim 50–70%, especially over equatorial regions. Compared to changes in functionalization and fragmentation, our results illustrate that the decrease in SOA in the upper troposphere is dominated by photolytic loss. While functionalization-fragmentation branching ratio strongly affects CCN in the lower troposphere, photolysis exerts a greater influence on CCN at higher altitudes (Figure S6e and S6f).

Although the model suggests almost complete photolytic removal of SOA at high altitudes, recent studies showed that a significant fraction of SOA does not photolyze, and this nonphotolabile SOA depends on SOA composition (O'Brien & Kroll, 2019; Zawadowicz et al., 2020). Although not considered in this study, heterogeneous chemistry with OH radicals becomes slower at higher altitudes as OH concentrations (molecule cm^{-3}) decrease with altitudes (Figure S4b in the supporting information). In contrast, photolytic removal likely gets more efficient at higher altitudes. Future studies are needed to better characterize the variability in SOA loss rates due to photolysis and heterogeneous OH sinks.

3.2.3. The Empirical Treatment of SOA

In POAtSOA configuration, we assume an empirical treatment for BB, BF, and FF SOA formation. The global distribution of SOA is shown in Figure 2d. To account for missing GFED emissions, POA emissions in this configuration are first increased by a factor of 2.6, and then converted to SOA with an e -folding time scale of 1 day. The increased POA and short conversion time leads to peak values of SOA near POA source regions. Therefore, POAtSOA simulates large SOA burdens of 20–80 mg m^{-2} over Africa, South America, and Asia (Figure 2d). Similar spatial distributions of SOA for both model formulations: the empirical POAtSOA and the more complex VBS SOA treatments that explicitly treat gas-particle partitioning and multigenerational aging (e.g., FRAG50), indicate that the simulated SOA particularly near BB sources can be adequately represented even with an empirical parameterization. However, in remote regions, the different time scales of SOA formation and sinks lead to larger differences in the empirical POAtSOA treatment compared to more explicit processes represented with the VBS treatments.

Although the result of lumping BB, BF, and FF sources in the POAtSOA treatment will increase anthropogenic FF OA when these lumped emissions are multiplied by a factor of 2.6, some of this increase in FF OA is expected due to formation of anthropogenic SOA, which is empirically treated in the POAtSOA scheme. Over FF-dominated regions, the assumption that increases FF POA by a factor of 2.6 causes a moderate (10–30%) bias compared to the multigenerational chemistry treatment of semivolatile organics in FRAG50_PHO. For example, supporting information Figure S7 compares the differences in simulated OA (sum of POA and SOA) burden between POAtSOA and FRAG50_PHO scenarios. Compared to FRAG50_PHO, POAtSOA predicts \sim 10–30% higher OA in FF-dominated regions of Central and Eastern United States, North China, and South Asia.

POAtSOA displays large peaks of SOA (up to $3 \mu\text{g kg}^{-1}$) over tropical regions below 700 hPa (Figure 3d). Compared to FRAG50, POAtSOA simulates a similar vertical structure of SOA but a stronger decrease in SOA concentrations in the middle and upper troposphere (Figures 3b and 3d). This stronger decrease can be explained a faster increase of OA near-source regions in POAtSOA due to instantaneous upscaling of POA emissions by a factor of 2.6 and their 1-day time scale conversion to SOA to account for additional OA, compared to FRAG50. This particle-phase OA can be also easily removed near their sources via wet

scavenging. Note that FRAG50 does not upscale particle-phase POA, but additional IVOC (equal to 4 times POA) are added in gas-phase within FRAG50 which take longer for SOA formation via multigenerational chemistry.

Compared to FRAG50, POAtSOA simulates similar magnitude of CCN concentrations in the lower troposphere. However, in the middle and upper troposphere (above 500 hPa), POAtSOA predicts ~10–20% lower CCN concentrations than those in FRAG50 (Figure S6b, d). The higher SOA-related CCN in remote regions within FRAG50 is due to slower multigenerational aging and SOA formation over larger spatial and temporal scales within VBS treatments compared to the empirical POAtSOA treatment.

4. Model Evaluation

In this section, we compare model simulations with observations in different areas around the globe. Investigating different regions is essential to evaluate the model's ability to represent both regional SOA concentrations and transport away from source regions.

4.1. Comparison With MODIS AOD

Satellite AOD is an indicator of all aerosol types, but aerosols below cloud decks cannot be seen by satellites. Although there is a persistent stratocumulus cloud deck in the southeast Atlantic Ocean, a recent field study during the ObseRvations of Aerosols above CLouds and their intEractionS (ORACLES-2016) showed that BB aerosols were mostly in the free troposphere above the cloud decks, hence satellite AOD is still a good indicator of these aerosols at high altitudes (Pistone et al., 2019), but could be variable depending on meteorology in different regions and times. In addition, since this work focuses on OAs, we evaluate model predictions of AOD against AOD retrievals from the MODIS on the Terra and Aqua satellites (Levy & Hsu, 2015) over regions dominated by BB OAs.

Over Africa, BB OAs are a significant source of POA, SOA, and SOA precursors (S/IVOCs) during the dry season from May to October. The simulated AOD at 550 nm captures both the spatial pattern and magnitude of large AOD values over central Africa and regions downwind for FRAG75, FRAG50_PHO, and POAtSOA, compared to the regional 10-year averaged MODIS AOD for the dry season between 2005 and 2014 (Figures 4a, 4b, 4d, and 4e). The moderate fragmentation configuration (FRAG50), however, significantly overestimates AOD in this region (Figure 4c).

In order to evaluate the simulated OA evolution from source and outflow regions, we compare modeled and satellite derived estimates of both absolute values of AOD and ratio of AOD at the each of consecutive outflow regions (labeled 1, 2 and 3 in Figure 4a) to the source region (also labeled in Figure 4a). Compared to MODIS AOD and FRAG75 simulation, the FRAG50 configuration without photolysis overestimates absolute AOD significantly both near-source and downwind regions (Figure 4f), although the FRAG50 simulated ratio of downwind to source AOD agrees better (compared to FRAG75) with MODIS (Figure 4g). In FRAG75, the ratio of downwind to source AOD is similar to MODIS ratio in Region 1, but higher than MODIS farther downwind (Regions 2 and 3, Figure 4g). Thus, FRAG75 causes lower SOA formation near source but increasingly higher SOA formation downwind, that is, ratio of downwind to source AOD is higher than MODIS over downwind Regions 2 and 3, Figure 4g. In comparison, FRAG50 causes too much SOA formation both over source and downwind regions. This evaluation indicates that a metric that combines both diagnostics: absolute AOD and downwind-to-source AOD ratios is needed for model evaluation with satellite AOD. Including photolysis within the model, the FRAG50_PHO configuration agrees best with both absolute MODIS AOD and AOD ratios (Figures 4f and 4g). Although the empirical POAtSOA also agrees with absolute MODIS AOD, it overestimates the ratio of downwind to source AOD over the outflow Regions 2 and 3 in Figure 4g. Note that the photolytic loss of SOA in FRAG50_PHO dramatically decreases the contribution from SOA to the total AOD from 60% (over source area) to 23% (over downwind Region 3, Figure S8c). In contrast, simulated SOA from FRAG75 and POAtSOA contribute more than 40% to total AOD in downwind regions (Figure S8a, d), indicating that these formulations overestimate the long-range transport of SOA in the SE Atlantic Ocean downwind African sources when SOA photochemical removal is neglected. Despite the potential wet removal of aerosols in the model, all model formulations without photolysis overestimates the ratio of downwind to source AOD (Figure 4g). This is likely due to BB aerosols being mostly above cloud decks in this region, (e.g., as observed during the ORACLES 2016 field campaign)

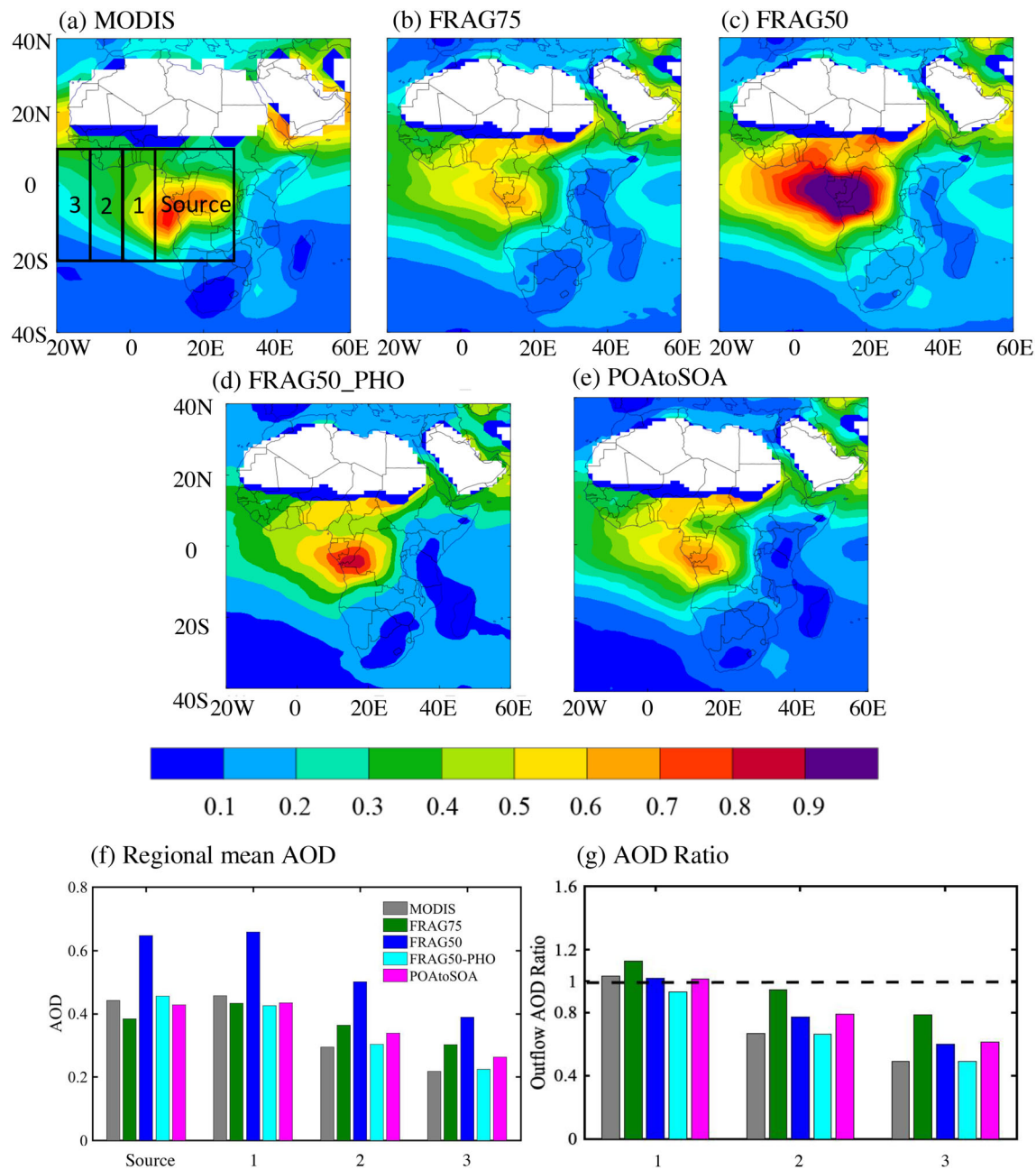


Figure 4. The spatial distribution of (a) MODIS AOD, and the model-predicted AOD from the (b) FRAG75, (c) FRAG50, (d) FRAG50_PHO, and (e) POAtSOA. The black box represents the high concentration source region, and the downwind Regions 1–3 corresponding to South African outflow during the biomass burning time of May–October for measurements. (f) Regional mean AOD averaged across each of source and downwind regions, and (g) ratio of each of downwind region median AOD to source region AOD. Median values of AOD over each region are used to calculate the outflow AOD ratio.

so that wet removal in clouds is not an efficient removal mechanism. An efficient sink of OAs, like photochemical removal of SOA is needed to explain MODIS AOD ratios shown in Figure 4g.

4.2. Comparison With Surface Observations

4.2.1. AMS Surface Measurements

To evaluate the simulated OA in E3SMv1, we select 17 surface AMS OA measurements between 2000–2008 from different field campaigns in rural/remote areas around the world (Zhang et al., 2007). The monthly averaged OA observations (including both hydrocarbon-like OA [HOA] and OOA) are used to compare with simulated OA (sum of POA and SOA). In addition, we also compare model SOA to observed OOA. Since the

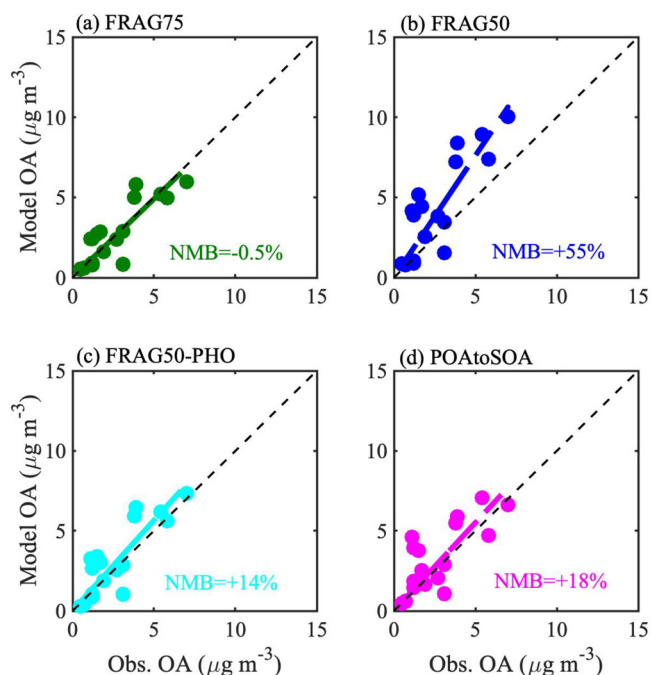


Figure 5. Scatterplots compare simulated campaign-average surface OA concentrations from (a) 75% fragmentation configuration FRAG75, (b) 50% fragmentation configuration FRAG50, (c) 50% fragmentation and photolysis loss SOA configuration FRAG50_PHO, and (d) the empirical SOA treatment configuration POAtSOA to AMS OA (sum of HOA and OOA) measurements at multiple sites throughout the world (Jimenez et al., 2009; Zhang et al., 2007). Only rural/remote sites are used, while the NMB are the normalized mean bias between simulated and measured OA concentrations.

AMS only samples aerosols less than $1 \mu\text{m}$, we use the simulated OA/SOA in Aitken ($<0.05 \mu\text{m}$), accumulation ($<0.5 \mu\text{m}$), and primary carbon ($<0.1 \mu\text{m}$) modes for comparison, while the simulated OA/SOA aerosols in coarse mode ($1\text{--}4 \mu\text{m}$, contributed an average of 5% to the total OA near surface) are out of measured range.

Among our four model treatments, the FRAG50_PHO and the empirical POAtSOA treatments agree best with global AMS measurements. The model-estimated OA for FRAG75 during the same months and locations of the measurements agrees best with observations of global OA concentrations, with a normalized mean bias (NMB) of -0.5% (Figure 5a). The FRAG75 formulation likely compensates errors in total OA by overestimating POA and underestimating SOA (Figure 6a). Note that FRAG75 significantly underestimates SOA downwind of anthropogenic source regions (Figure 6a, light green spots) including Okinawa Island and Fukue Island, Japan (downwind of China); QUEST and Hyytiälä, Finland (downwind of West and North Europe); and Pinnacle State Park, New York (downwind from New York City). Compared to FRAG75, FRAG50 simulates higher SOA concentrations (NMB = $+24\%$) and shows better agreement with measurements (Figures 6a and 6b). However, FRAG50 largely overestimates observed OA by 55% (Figure 5b).

With a strong production (e.g., strong functionalization) and a strong sink of SOA, the FRAG50_PHO agrees best with observations (including those downwind of major anthropogenic sources) for both simulated OA and SOA, with NMB values of $+14\%$ and -19% , respectively (Figures 5c and 6c), indicating that the photolytic loss of SOA improves simulated surface OA concentrations globally in E3SMv1.

The empirical POAtSOA formulation also captures the magnitude for both observed OA and SOA (Figures 5d and 6d). In this configuration, POA emissions are increased by a factor of 2.6, and the simulated OA is

slightly overestimated (NMB = $+18\%$), consistent with previous modeling studies that suggest POA emissions from BB should be increased by a factor of 2–3.4 to match the measurements in global models (Sakaeda et al., 2011; Tosca et al., 2013). However, these previous studies did not include prognostic SOA treatments. Thus, similar to FRAG50_PHO, POA to SOA agrees with surface-based total OA and OOA measurements globally. Note that most surface AMS measurements were too close to sources, therefore most model treatments that form SOA on the time scales of ~ 1 day likely agree with these observations.

4.2.2. IMPROVE Network OC Observations

IMPROVE (<http://vista.cira.colostate.edu/Improve/improve-data>) program provides OC concentrations in national parks, monuments, and wilderness areas around the United States. A monthly comparison of model predictions with 165 sites in rural and remote areas (excluding sites near large urban areas) of OC measurements between 2007 and 2011 are shown in Figure 7. Note that IMPROVE OC represents sum of POA and SOA, therefore, model simulated total OC (obtained by dividing OA by OA/OC ratio) needs to be evaluated with IMPROVE measurements. Observed monthly medians, 15th, and 85th percentiles are shown as boxes, indicating site-to-site variability for each month. In order to convert the model simulated OM to the observed OC concentration, we use an OA/OC ratio of 1.6 and 2.1 for POA and SOA, respectively. The OA/OC ratio is consistent with recent studies that reported values of 1.6 for BB POA (Andreae, 2019; Canagaratna et al., 2015), and is within the range reported (1.6 and 2.1) for BG SOA and rural mixed OA, respectively (Malm et al., 1994; Schroder et al., 2018; Shilling et al., 2009; Turpin & Lim, 2001; Zhang et al., 2005). In this study, the simulated OA (sum of POA and SOA) is calculated as the sum of OA in Aitken, accumulation, and primary carbon modes to facilitate comparison with the measurements of fine-mode particles ($<1 \mu\text{m}$).

All configurations capture the seasonal variations of OC in the United States, with peak OC values in the summer and minimum values during winter (Figure 7). For all simulations, POAtSOA shows the lowest

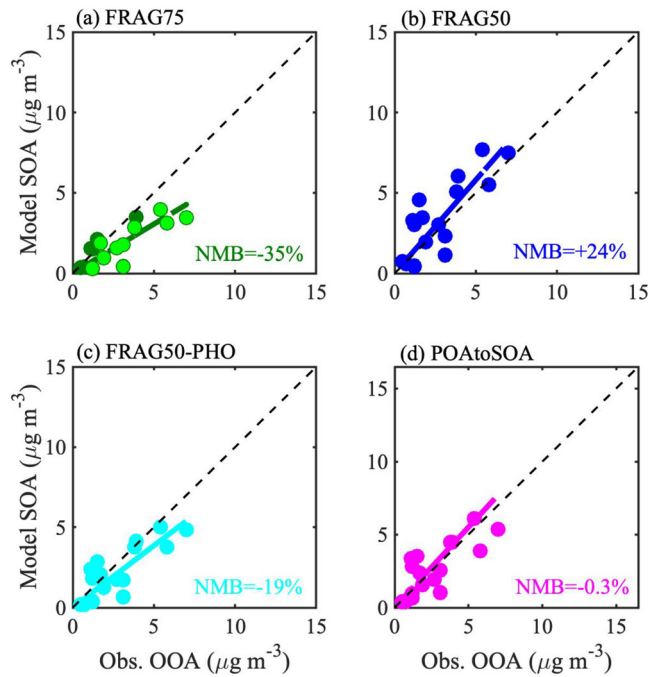


Figure 6. The same as Figure 8 but for predicted SOA and measured OOA. The light green spots in (a) represent the comparison in downwind of anthropogenic source regions including Okinawa Island and Fukue Island, Japan (downwind of China); QUEST and Hyttiala, Finland (downwind of west and north Europe); and Pinnacle State Park, New York (downwind from New York City).

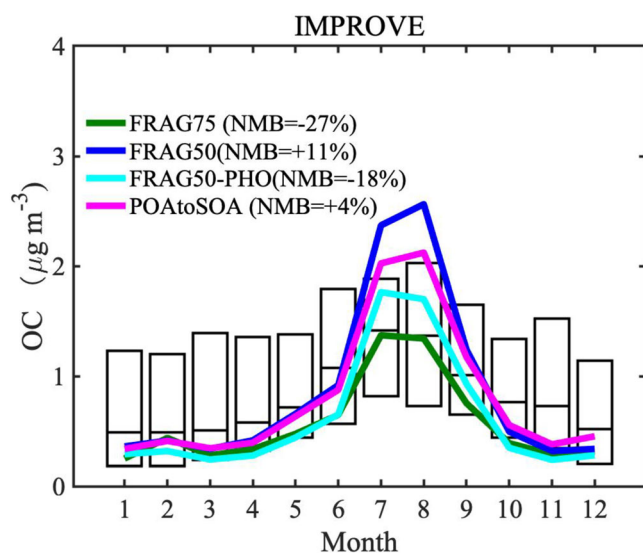


Figure 7. Observed and simulated monthly average OC concentrations from the 165 Interagency Monitoring of Protected Visual Environments (IMPROVE) sites in the United States. The boxes represent the observed median, and the 15th and 85th percentiles denote the site-to-site variability. The colored lines correspond to median values of corresponding model-predicted OC concentrations. Normalized mean biases (NMB) are calculated throughout the year.

overall bias compared to measurements across all seasons due to compensating overprediction during summer and underprediction during the other seasons (NMB = +4%). Modeled OC bias compared to IMPROVE measurements varies seasonally as POAtoSOA and FRAG50 significantly overestimate OC concentrations in summer, but underpredict OC during the other seasons (Table S2). However, both FRAG75 and FRAG50_PHO agree with observed summertime OC concentrations from June to September (NMB = -9% and +9%, respectively, Table S2). Note that there is often a low bias in the IMPROVE OC data for the summer months, mostly due to evaporation from filters (Kim et al., 2015), which likely indicates that the FRAG50_PHO simulation is likely closer to the real OC profile (if the summertime bias in the measurements is accounted for).

4.3. Comparison With Aircraft Observations

Most satellite products (like MODIS) only provide column integrated indicators of aerosol amounts. However, in order to diagnose aerosol effects on clouds and radiation, knowledge of the vertical profiles of aerosols is necessary. A three-dimensional global atmospheric model like E3SM is able to simulate aerosol vertical profiles, but it is important to evaluate the simulated profiles with direct in situ observations. Although aircraft sample a limited spatial and temporal extent, they are critical for evaluating model simulations. In this section, we evaluate OA simulations with aircraft campaigns conducted over the Arctic/sub-Arctic, midlatitude, and tropical regions (Cubison et al., 2011; Hodzic et al., 2020; Jacob et al., 2010; Martin et al., 2016; Shilling et al., 2018; Wendisch et al., 2016). The different aircraft campaigns are influenced by different OA sources depending on their sampling season and region. For example, while the NASA Arctic Research of the composition of the Troposphere from Aircraft and Satellite (ARCTAS) aircraft field summer campaign (ARCTAS CARB/B, June–July of 2008) targeted the evolution of wildfire plumes in middle to high latitudes (e.g., North America and Eurasia), the spring campaign (ARCTAS-A, April of 2008) targeted long-range transport of pollutants and hence is suited to investigate the impacts of SOA treatment on OA far from sources (Cubison et al., 2011; Jacob et al., 2010). Over tropical regions, the Green Ocean Amazon (GoAmazon) 2014/5 field campaign is heavily influenced by local and regional forest BB during the summer/dry season (Martin et al., 2016; Shilling et al., 2018; Wendisch et al., 2016), while the Aerosol, Cloud, Precipitation, and Radiation Interactions and Dynamics of Convective Cloud Systems-Cloud processes of the main precipitation systems in Brazil: A contribution to cloud resolving modeling and to the Global Precipitation Measurement (ACRIDICON-CHUVA) campaign conducted with the German High Altitude and Long-Range Research Aircraft (HALO) from September to October 2014 (Wendisch et al., 2016) sampled farther downwind regions and regional OA less affected by BB during the dry BB season. In contrast, the GoAmazon field campaign measurements during the wet season (February–March) were mostly devoid of BB and sampled the anthropogenic urban outflow from Manaus mixing with regional BG emissions (Martin et al., 2016; Shilling et al., 2018).

We also evaluate model predictions with the first two ATom campaigns during July–August of 2016 (ATom-1) and January–February of 2017 (ATom-2) which systematically sampled the remote marine troposphere with a highly instrumented chemistry package that included fast OA

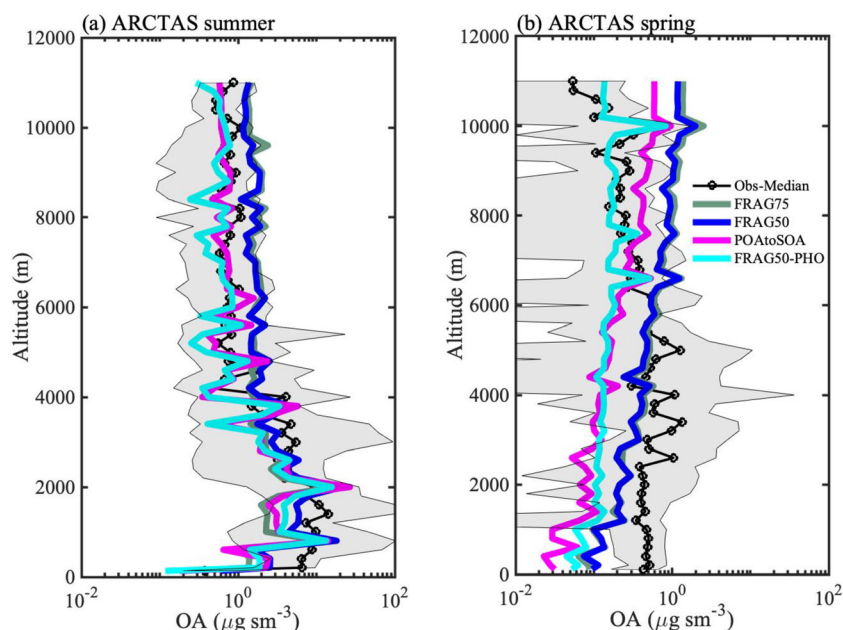


Figure 8. Median vertical profiles comparing the observed (black) and simulated (colored) OA mass concentrations from ARCTAS (a) summer campaign and (b) spring campaign. The gray shading denotes the 10th and 90th percentiles of the measurements. The profiles are binned at 200 m intervals from the surface to 12 km.

measurements. We separate the ATom campaigns into three datasets in order to distinguish between remote marine: the equatorial ocean between 30°S and 30°N, the southern midlatitude ocean between 60°S and 30°S and continental regions (e.g., North America).

The model outputs relevant data along the aircraft flight transects during the same days as the aircraft flight sampling. The median values of observed and simulated OA are used for comparison, with the 10th and 90th percentiles of observed OA representing the sampling variability for each campaign. For every 200 m from

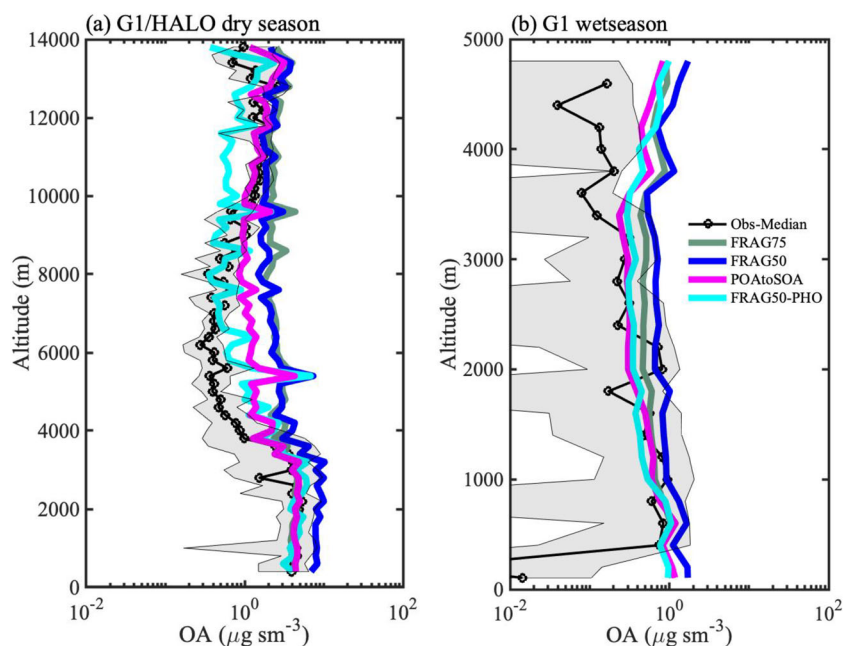


Figure 9. Median vertical profiles comparing the observed (black) and simulated (colored) OA mass concentrations from the G-1 and HALO aircrafts during (a) dry season and (b) wet season. The gray shading denotes the 10th and 90th percentiles of the measurements. The profiles are binned at 200 m intervals from the surface to 14 km.

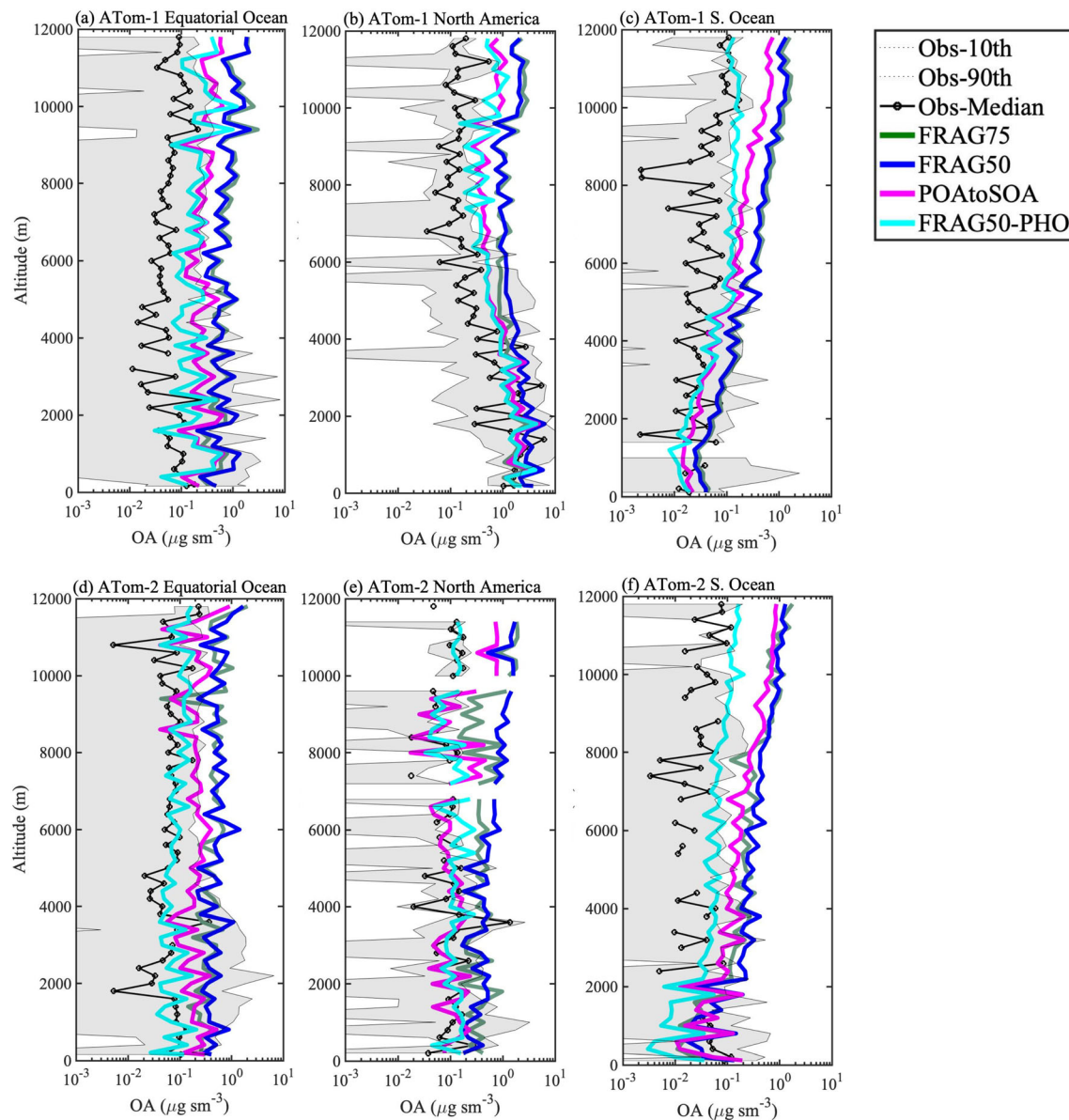


Figure 10. Median vertical profiles comparing the observed (black) and simulated (colored) OA mass concentrations over equatorial ocean (a, d), North America (b, e), and South Hemisphere ocean (c, f) from ATom summer (ATom-1, a–c) and winter (ATom-2, b–f) campaigns. The gray shading denotes the 10th and 90th percentiles of the measurements. The profiles are binned at 200 m intervals from the surface to 12 km.

the surface to 11–14 km, we calculate the median OA concentration for both the observations and our simulations; each point on Figures 8–10 corresponds to the median value of each 200 m layer.

4.3.1. ARCTAS Campaigns

During the ARCTAS summer campaign (Figure 8a), both FRAG75 and FRAG50 overpredict OA loadings in the middle and upper troposphere (above 4 km). FRAG50_PHO illustrates how including the photolytic loss of SOA greatly improves the vertical profile of simulated OA over Arctic BB regions compared to FRAG50. In the middle and upper troposphere, where high SOA loadings dominate the total OA loadings in both FRAG75 and FRAG50, the photolytic loss mechanism in FRAG50_PHO reduces simulated OA by 30–80%. Therefore, the contributions of SOA (mostly due to BB) to the total OA loadings are decreased from 86–94% in FRAG50 to 46–85% in FRAG50_PHO, due to the efficient removal of SOA by photolysis in the middle and upper troposphere. Similar to FRAG50_PHO, the empirical POAtoSOA treatment also agrees better with measured OA in the middle and upper troposphere during the summertime compared to FRAG50 and FRAG75.

During the springtime, long-range transport of fire emissions from eastern Siberia and Russia impacted observed OA concentrations, especially above 2 km (Jacob et al., 2010; Shrivastava et al., 2015; Warneke et al., 2010). Below 7 km altitudes, FRAG75 and FRAG50 agree much better with observed OA, while both FRAG50_PHO and POAtoSOA significantly underestimate OA. However, at higher altitudes above 7 km, FRAG75 and FRAG50 overpredict OA while FRAG50_PHO agrees better with measurements. These comparisons suggest the large variability in BB emissions, and their long-range during the springtime over the Arctic in the model.

4.3.2. GoAmazon and ACRIDICON-CHUVA Campaigns

Both GoAmazon2014/5 and ACRIDICON-CHUVA field campaign were conducted over the Amazonian rainforest. These campaigns included measurements collected onboard the DOE G-1 and HALO research aircrafts; flights across the Amazon basin (Martin et al., 2016; Schulz et al., 2018; Shilling et al., 2018; Wendisch et al., 2016). The HALO aircraft flew up to altitudes of 15 km, while the G1 aircraft flights were limited to <5 km altitude. The AMS measurements in the lower troposphere during ACRIDICON-CHUVA campaign were biased low due to reduced instrument transmission for larger aerosols documented by (Mei et al., 2020), therefore, we combined data from GoAmazon 2014/5 (0–4 km) and from ACRIDICON-CHUVA (above 4 km) for the dry season to understand the impact of BB on local OA concentrations over the Amazon region.

During the Amazon dry season (Figure 9a), all configurations except FRAG50_PHO overpredict OA loadings in the middle and upper troposphere (above 4 km). FRAG50_PHO illustrates that a strong production (e.g., low fragmentation and high functionalization) and a strong sink of SOA (e.g., particle-phase photolysis) greatly improves the vertical profile of simulated OA over the tropical BB regions compared to all other model formulations (FRAG75, FRAG50 and POAtoSOA). In the lower troposphere (below 4 km), the simulated OA is more sensitive to the functionalization/fragmentation branching ratio in tropical regions compared to the high-latitude regions of the Arctic. For example, compared to FRAG75, FRAG50 predicts an increase in OA by a factor of 2.5 in the boundary layer over the Amazon Basin (Figure 9a), much larger than the predicted FRAG50/FRAG75 ratio of ~1.5 over central/northern Canada and Siberia (Figure 8a). Since the ambient temperatures are very different (e.g., -10°C for ARCTAS spring and $>30^{\circ}\text{C}$ for the Amazon dry season), a greater fraction of semivolatile precursors partitions to SOA in the Arctic regions in both FRAG75 and FRAG50 (reducing their intermodel differences in simulated SOA) compared to the warm tropics. Thus, SOA formation is more sensitive to the functionalization-fragmentation branching ratio over the warm tropics compared to the Arctic.

OA loadings during the wet season in the Amazon are about 1 order of magnitude lower than the dry season. SOA formation during the wet season is mainly governed by BG SOA and anthropogenically enhanced BG SOA (Shrivastava et al., 2019). Due to the relatively coarse resolution of the global models (compared to high resolution regional models), fine-scale features in SOA chemistry and their removal may not be adequately resolved. Almost all model configurations show reasonable agreement with OA measurements below an altitude of 1 km, since most SOA is freshly formed near sources. As discussed earlier, most SOA treatments derived from chamber measurements with SOA formation time scales of less than 1 day are expected to reasonably capture fresh SOA formation at low altitudes. Between altitudes of 1–3 km, FRAG50 and FRAG75 predict OA closer to the median of observations, while FRAG50_PHO and POAtoSOA often underpredict OA. At higher altitudes, FRAG50 often overpredicts OA. The wet-season Amazon is one of the most challenging regions for modeling SOA formation due to large uncertainties in emissions of BG VOCs, knowledge of how SOA chemical production and sinks vary with altitudes, and a complex convective and wet scavenging environment (Guenther et al., 2006, 2012; Jokinen et al., 2015; Rasch et al., 2019; Shrivastava et al., 2019). It is likely that both a stronger SOA source and a stronger sink, as in the FRAG50_PHO configuration, is needed to compensate for errors in modeled convective transport and wet removal over the wet-season Amazon.

4.3.3. ATom Campaigns

ATom-1 (summer) and ATom-2 (winter) campaigns are used to investigate the impacts of different SOA treatment on OA sampled far away from sources over tropics and midlatitude to high-latitude regions. Figure 10 compares the vertical profiles of simulated OA from all configurations with measured OA over tropical ocean, Southern Hemisphere ocean (Southern Ocean), and North America. Only FRAG50_PHO captures the observed vertical structure of OA concentrations in all of equatorial ocean, the Southern Ocean, and North America, while the simulated OA from other configurations largely overestimate mea-

Table 3
Summary of the Average Radiative Effects in PD and PI for Each SOA Treatment

		FRAG75	FRAG50	FRAG50_PHO	POAtSOA
Radiation effect (W m^{-2}) (PD) at TOA	REari (SOA) TOA	-1.52	-1.97	-0.65	-1.22
	REari (SOA) surface	-2.46	-3.14	-1.05	-1.94
	REaci (SOA) atmosphere	+0.94	+1.17	+0.4	+0.72
	REari (All aero) TOA	-3.66	-4.16	-2.78	-3.29
	REaci	-22.34	-22.61	-22.71	-23.06
Effective radiation forcing (W m^{-2}) (PD-PI) at TOA	RFari (SOA)	-0.31	-0.42	-0.08	-0.001
	RFari (All aero)	-0.63	-0.79	-0.43	-0.31
	RFaci	-1.27	-1.23	-1.24	-1.02

sured OA above 5 km (Figure 10). Since SOA wet removal rates and lifetimes are expected to vary from one region to another and also temporally, we calculated SOA removal rates and lifetimes over rectangular regions bounding all the ATom-1 and ATom-2 aircraft transects during the summer and winter, corresponding to each of the four panels of Figure 10. Supporting information Table S3 shows that different SOA model formulations cause large variations in simulated SOA lifetimes, depending on the contribution of wet removal to the total sinks. FRAG75 predicts the greatest overall SOA lifetimes of 12.5–25.4 days (wet removal lifetimes of 13.3–27.8 days) over equatorial oceans, the Southern Ocean, and North America during ATom-1 and ATom-2, while FRAG50_PHO predicts the smallest overall lifetimes of 2–4 days (wet removal lifetimes of 4.6–14.3 days). This result shows that even within the same model with given physics and cloud convective treatments, different SOA formulations can cause a factor of 2–3 differences in SOA wet removal lifetimes. FRAG75 predicts the greatest SOA lifetimes of 25.4 days over the Southern Ocean during the wintertime ATom-2, while the smallest lifetime of 12.5 days is simulated over the Southern Ocean during ATom-1. Compared to the simulated SOA lifetime of 8.6–16 days in FRAG50, photolysis reduces SOA lifetime to 2–4 days within FRAG50_PHO. This indicates that photolysis is a much stronger sink of SOA compared to wet removal during ATom-1 and ATom-2 field campaigns. While wet removal contributes to 82–85% of SOA loss rates in FRAG50 configuration over ATom campaign regions, it only contributes 29–34% in FRAG50_PHO configurations over equatorial ocean and 34–38% over North America (Table S3 in the supporting information). In contrast, photolytic removal dominates SOA loss (54–64%) in these regions. Note that although secondary activation treatment of aerosols above the cloud base in E3SMv1 is already included, it has minor effect on vertical distributions of SOA (Yu et al., 2019). Since regions at higher altitudes (above 5 km) are mostly unaffected by wet removal, additional chemical sinks of SOA such as photolysis, or heterogeneous oxidation with OH radicals (not included here) are critical to explain SOA formation and transport source to downwind regions in free troposphere, consistent with section 4.2.

5. SOA-Induced Changes in Aerosol Direct Radiative Effect and Cloud Radiative Forcing

The various SOA formulations affecting the horizontal and vertical distributions of aerosols result in differences in the interaction with shortwave and longwave radiation. The radiative effect due to aerosol-radiation interaction (REari) directly impacts Earth's energy balance. In PD (year 2014) simulations, the SOA REari is diagnosed as the difference between the net clear-sky radiative flux at the top of atmosphere (TOA) calculated with and without SOA within the same simulation (Heald et al., 2014). Figure S9 shows the spatial distributions of the SOA-induced REari at TOA from the different SOA treatments. All SOA model formulations consistently predict a large negative REari in the range of -4 to -12 W m^{-2} around the BB/BG source regions of Central and South Africa, South America, and North America, as well as the industrial regions of Asia. However, away from source and downwind regions and over the oceans, the cooling effect of SOA decreases from $\sim -2 \text{ W m}^{-2}$ (FRAG75 and FRAG50) to -0.5 W m^{-2} (FRAG50_PHO) since photolysis almost completely removes SOA over remote oceans. FRAG50_PHO, which captures the vertical distribution of OA best, predicts a global annual mean SOA REari of -0.65 W m^{-2} for clear-sky conditions, similar to the global annual mean OA REari (-0.61 W m^{-2}) reported in Heald et al. (2014). The contribution of SOA to the total REari is 23% in FRAG50_PHO, much lower than 37–47% from other configurations. The difference in REari between PD and PI is referred to as RFari. Table 3 shows that different SOA model configurations predict large

differences among RFari (PD-PI). FRAG50 and FRAG75 predict the strongest SOA RFari of -0.42 and -0.31 W/m^2 respectively. Including photolysis greatly reduces the PD-PI RFari from -0.42 in FRAG50 to -0.08 W/m^2 in FRAG50_PHO. Thus, photolysis reduces estimates of direct radiative cooling effects of SOA from PD to PI. Moreover, the total aerosol (all aerosols including OA and inorganic aerosols) RFari is estimated as -0.43 W m^{-2} for clear-sky conditions from FRAG50_PHO, and SOA accounts 19% of this RFari. In comparison, SOA contributes to $\sim 50\%$ of RFari in both FRAG50 and FRAG75 configurations, and consequently lead to stronger cooling than those in FRAG50_PHO.

The POAtoSOA formulation shows the smallest PD-PI OA RFari of -0.001 W/m^2 , which is surprising given the large differences in POA emissions, that is, a total of 122.5 Tg/yr POA for PD (BF + FF: 67.1 Tg, BB: 55.4 Tg), and a total of 66.3 Tg/yr POA for PI (BF + FF: 15.4 Tg, BB: 50.9 Tg). Note that in this empirical treatment, increased POA emissions are converted to SOA at an e -folding time scale of 1 day. The small PD-PI RFari in this treatment is likely to the similar vertical profile of BB aerosols in middle and upper troposphere in many regions, globally. While BF + FF POA is a factor of 4 higher in PD than PI, it has much smaller influence on global RFari likely because it is concentrated in a few regions like East Asia, and also due to compensating changes from BG SOA. Due to changes in land use and climate change, in this study, the monoterpenes emissions are estimated to decrease by a factor of ~ 1.8 from PI to PD conditions, that is, from 144 (PI) to 82 Tg/yr (PD). But isoprene emissions are estimated to depict a minor increase of $\sim 10\%$ in PD, that is, from 486 (PI) to 537 Tg/yr (PD). The decrease in monoterpene emissions would substantially decrease BG SOA formation. In comparison, BB POA is very similar between PD and PI and is distributed over larger source regions. Thus, similar BB POA, and compensating changes due to increases in BF + FF POA + anthropogenic SOA and decreases in BG SOA minimizes PD-PI RFari in POAtoSOA.

Table 3 shows that the difference between SOA REari at the TOA and surface is positive in all model configurations, indicating that SOA has a significant warming component in addition to scattering. The SOA warming component is substantial, that is, 0.94, 1.17, 0.4, and 0.72 W/m^2 for FRAG75, FRAG50, FRAG50_PHO and POAtoSOA, respectively and are larger than Shrivastava et al. (2015), likely due to larger SOA burdens compared to that study. Note that SOA has a small absorbing component although its imaginary refractive index is assumed to be 40 times lower than BC. But over high latitudes like the Arctic, SOA dominates simulated aerosol composition, and contributes 90% to total aerosols. Moreover, light-absorbing organics have been detected in several campaigns over polar regions, outflow of Africa and North America (Lee et al., 2020; Zeng et al., 2020).

In PD simulations, the change in cloud radiative forcing due to aerosol-cloud interactions (REaci) is diagnosed from the shortwave and longwave cloud forcing within the same simulation. All model configurations predict global annual mean net cloud radiative forcing in the range of -22.3 – 23.1 W m^{-2} (Table 3). With a stronger SOA source, FRAG50 leads to an increase in CCN concentrations in the lower troposphere (below 600 hPa), and consequently enhances cooling effect of -0.3 W/m^2 in PD (difference between REaci of FRAG50 and FRAG75, reported in Table 3). Photolytic removal of SOA largely reduces CCN concentrations in FRAG50_PHO compared to FRAG50, especially over the equatorial ocean and in the upper troposphere (Figure S6f). This change in CCN translates to a difference in PD REaci of all aerosols of -0.1 W/m^2 (difference between REaci of FRAG50_PHO and FRAG50 in Table 3). Note that the E3SM model treats nucleation due to sulfuric acid (Liu et al., 2012) but does not explicitly include organic-mediated nucleation that could be important at high altitudes in BG-dominated regions (Ranjithkumar et al., 2020; Sengupta et al., 2020; Sporre et al., 2020; Zhao et al., 2020; Zhu et al., 2019). The differences in CCN predictions among our different model formulations reflect effects of changes in SOA growth with varying multigenerational chemistry formulations of SOA. Future planned developments in E3SM will include an additional nucleation mode and organic-mediated nucleation based on Zhao et al. (2020).

The total change in radiative forcing of -0.01 W/m^2 between PD and PI from aerosol-cloud interactions (RFaci) is even smaller from FRAG50_PHO than other scenario. Our results agree with Tilmes et al. (2019) who also reported a minor change in cloud forcing with changes in SOA chemistry. The small sensitivity of REaci to the SOA chemistry treatment is partly due to the assumption that SOA is internally mixed with other aerosol components in the same mode in E3SMv1. Compared to the internally mixing assumption, Zhu et al. (2017) reported that the global RFaci is enhanced by ~ 0.7 W m^{-2} when treating SOA as an external mixture with other components. Their results suggest that the global RFaci could be even larger if the aerosol

treatment in E3SM considered both externally and internally mixed SOA, with amounts of each determined by relevant processes. Our results show a stronger cooling than the E3SMv1 standard version of -1.13 W m^{-2} (Wang et al., 2020).

6. Discussion and Conclusions

Using the global E3SMv1 model, we have examined the impacts of SOA treatments on SOA spatial distribution and lifetime through (1) functionalization/fragmentation reactions, (2) photochemical removal, and (3) an empirical SOA parameterization. The analysis helps in evaluating the implications of the uncertainties in simulated OA in a global model, as well as their radiative effect.

Our primary findings are as follows:

1. The branching ratio between fragmentation and functionalization that governs the multigenerational aging of gas-phase SOA precursors greatly impacts the source term of SOA and its long-range transport. Decreasing fragmentation with an increase in functionalization reactions results in a stronger source of SOA.
2. Both a strong production (e.g., strong functionalization in the current treatment) and a strong sink of SOA (e.g., particle-phase photolysis) in addition to wet and dry deposition are needed to reproduce the vertical OA profiles measured during several aircraft field campaigns (DOE Green Ocean Amazon (GoAmazon2014/5), the ACRIDICON-CHUVA field campaign, ATom 2016/2017, and the NASA ARCTAS 2008). During summertime, our SOA treatment with moderate fragmentation and photolysis (FRAG50_PHO) shows low bias compared to the surface-based IMPROVE network OC measurements, while neglecting photolysis (FRAG50) significantly overpredicts OC during summer. Also, a comparison with aircraft measurements shows that our SOA treatments that do not include photolysis consistently overpredict SOA in the middle and upper troposphere. A strong sink of SOA, like photolysis, is needed to reproduce OA loadings over the SE Atlantic Ocean downwind African BB regions where BB aerosols are above cloud decks, and at higher altitudes over other regions where wet removal sinks are small. However, additional measurements are needed to further constrain photolytic loss of different SOA types under atmospherically relevant meteorological and chemical regimes, especially at high altitudes and differing levels of NO_x .
3. To account for recent field studies that suggest no increase in net OA formation over and downwind BB regions, we also test an empirical treatment of SOA formed through aging of combustion-derived organics that increases POA from BB and anthropogenic emissions near-source region and converts POA to SOA with an aging time scale of 1 day. This empirical treatment without explicit multigenerational aging of SOA precursors performs surprisingly well in simulating OA loadings near the surface as measured by AMS and IMPROVE network. However, the empirical treatment overestimates OA loadings in middle and upper troposphere compared to aircraft measurements, especially during the dry BB season of GoAmazon2014/5, and the wintertime ATom-2 field campaign flights over equatorial oceans and North America. Future studies should include the realistic SOA loss process (e.g., photolytic loss), which is not considered in POAtoSOA treatment. The model configuration that includes moderate 50% fragmentation and photolysis performs much better than the empirical treatment in these regions, and performs as well as the empirical treatment in other regions. Including additional photolytic removal of SOA in the empirical treatment would likely improve its predictions over these regions.
4. Differences in SOA treatments greatly affect the wet removal lifetimes of SOA due to differences in simulated horizontal and vertical distributions of SOA. Different SOA treatments also cause large variations in the simulated direct radiative forcing of all aerosols ranging from -0.43 (50% fragmentation and photolysis) to -0.79 W m^{-2} (50% fragmentation without photolysis). In contrast, three of the SOA formulations in this study predict very similar RFaci (calculated as the difference in cloud forcing between PD and PI simulations) likely due to cancelations of errors in SOA formulations. Since BB is the largest source of OA in this study and the differences in BB OA between PD and PI are not as large as other anthropogenic dominated aerosols, these simulations predict similar RFaci. However, the empirical treatment predicts $\sim 18\%$ weaker global RFaci compared to the explicit SOA formulations. The reason for the smallest RFaci is similar to the cancelation of PD-PI RFari of SOA in this treatment, due to (1) the similar vertical profile of BB aerosols and (2) a compensating effect of reducing BG SOA likely due

to reduction of monoterpene emissions in PD compared to PI conditions that offsets the increase of BF + FF POA + anthropogenic SOA in PD. Compared to the default E3SMv1 model (Wang et al., 2020), our explicit SOA treatment with fragmentation and photolysis agrees much better with OOA and IMPROVE OC measurements at multiple surface locations. Meanwhile, our new formulation agrees much better with aircraft-based OA measurements in the middle and upper troposphere compared to E3SMv1 default treatment, which likely overestimated OA concentrations at high altitudes. Our results provide important insights about how different SOA processes likely impact aerosol distributions and radiative forcing.

In addition, there are other factors that may result in an overestimation of OA, such as the uncertainties in cloud parameterizations and wet removal, SOA oxidation reaction rates, and aerosol transport. For example, Xie et al. (2018) suggested that cloud fraction in E3SMv1 is overestimated in the high latitudes but underestimated in middle latitudes, which may lead to a bias in precipitation.

The various SOA treatments significantly affect the Earth's energy balance. Photolytic removal reduces the lifetime and burden of SOA, especially, in the upper troposphere and over remote oceans and the Arctic. Therefore, our best case FRAG50_PHO predicts a PD global annual mean SOA RE_{air} of -0.65 W m^{-2} at TOA under clear-sky conditions. In addition, the total aerosol RF_{air} (the differences in RE_{air} between PD and PI) is estimated as -0.43 W m^{-2} for clear-sky conditions from FRAG50_PHO, while SOA accounts for about 19%. In comparison, FRAG50 predicts a stronger cooling with a total RF_{air} of -0.79 W m^{-2} , where half the cooling is attributed to SOA, but it is still within the forcing range estimated from AeroCom phase I and II experiments (Myhre et al., 2013; Schulz et al., 2006). Moreover, FRAG50_PHO, which captures the vertical distribution of OA best, predicts a stronger global mean RF_{air} (-1.24 W m^{-2}) compared to the E3SMv1 standard version of -1.13 W m^{-2} (Wang et al., 2020). These results highlight the importance of constraining SOA loadings for estimating Earth's energy budget. Future measurements and modeling are also needed to better constrain the photolytic and heterogeneous chemical removal of SOA at high-altitude atmospheric conditions.

Acknowledgments

This research is based on work supported by the U.S. Department of Energy (DOE), Office of Science, Office of Biological and Environmental Research (BER), Earth and Environmental System Modeling (EESM) program as part of the Energy Exascale Earth System Model (E3SM) project. Dr. Shrivastava was also supported by the U.S. DOE, Office of Science, Office of Biological and Environmental Research through the Early Career Research Program. The authors thank the G-1 flight and ground crews for supporting the GoAmazon 2014/5 mission. Funding for data collection onboard the G-1 aircraft and at the ground sites was provided by the Atmospheric Radiation Measurement (ARM) Climate Research Facility, a U.S. DOE Office of Science user facility sponsored by the Office of Biological and Environmental Research. The Pacific Northwest National Laboratory is operated for DOE by Battelle Memorial Institute under contract DE-AC06-76RL01830. Computational resources for the simulations were provided by the PNNL Institutional Computing (PIC) facility. We acknowledge Virendra Ghate for processing the 10 yr average MODIS AOD observations. J. L. J. and P. C. J. were supported by NASA NNX15AH33A and 80NSSC19K0124. Q. Zhang was supported by DOE ASR DE-SC0014620. P.C.-S. was supported by the U.S. Department of Energy by Lawrence Livermore National Laboratory under Contract DE-AC52-07NA27344.

References

- Aiken, A. C., Decarlo, P. F., Kroll, J. H., Worsnop, D. R., Huffman, J. A., Docherty, K. S., et al. (2008). O/C and OM/OC ratios of primary, secondary, and ambient organic aerosols with high-resolution time-of-flight aerosol mass spectrometry. *Environmental Science & Technology*, *42*(12), 4478–4485. <https://doi.org/10.1021/es703009q>
- Akagi, S. K., Craven, J., Taylor, J., McMeeking, G., Yokelson, R., Burling, I., et al. (2012). Evolution of trace gases and particles emitted by a chaparral fire in California. *Atmospheric Chemistry and Physics*, *12*(3), 1397–1421. <https://doi.org/10.5194/acp-12-1397-2012>
- Andreae, M. O. (2019). Emission of trace gases and aerosols from biomass burning—An updated assessment. *Atmospheric Chemistry and Physics*, *19*(13), 8523–8546. <https://doi.org/10.5194/acp-19-8523-2019>
- Atkinson, R., & Arey, J. (2003). Atmospheric degradation of volatile organic compounds. *Chemical Reviews*, *103*(12), 4605–4638. <https://doi.org/10.1021/cr0206420>
- Boffetta, P., Jourenkova, N., & Gustavsson, P. (1997). Cancer risk from occupational and environmental exposure to polycyclic aromatic hydrocarbons. *Cancer Causes and Control*, *8*(3), 444–472. <https://doi.org/10.1023/a:1018465507029>
- Boucher, O., Randall, D., Artaxo, P., Bretherton, C., Feingold, G., Forster, P., et al. (2013). Clouds and aerosols. In *Climate change 2013: The physical science basis. Contribution of Working Group I to the Fifth Assessment Report of the Intergovernmental Panel on Climate Change* (pp. 571–657). Cambridge University Press.
- Boyd, C. M., Sanchez, J., Xu, L., Eugene, A. J., Nah, T., Tuet, W. Y., et al. (2015). Secondary organic aerosol formation from the β -pinene +NO₃ system: Effect of humidity and peroxy radical fate. *Atmospheric Chemistry and Physics*, *15*(13), 7497–7522. <https://doi.org/10.5194/acp-15-7497-2015>
- Braman, T., Dolvin, L., Thrasher, C., Yu, H., Walhout, E. Q., & O'Brien, R. E. (2020). Fresh versus photo-recalcitrant secondary organic aerosol: Effects of organic mixtures on aqueous photodegradation of 4-nitrophenol. *Environmental Science & Technology Letters*, *7*(4), 248–253. <https://doi.org/10.1021/acs.estlett.0c00177>
- Brito, J., Rizzo, L. V., Morgan, W. T., Coe, H., Johnson, B., Haywood, J., et al. (2014). Ground-based aerosol characterization during the South American Biomass Burning Analysis (SAMBBA) field experiment. *Atmospheric Chemistry and Physics*, *14*(22), 12,069–12,083. <https://doi.org/10.5194/acp-14-12069-2014>
- Brock, C. A., Wagner, N. L., Anderson, B. E., Attwood, A. R., Beyersdorf, A., Campuzano-Jost, P., et al. (2016). Aerosol optical properties in the southeastern United States in summer—Part 1: Hygroscopic growth. *Atmospheric Chemistry and Physics*, *16*(8), 4987–5007. <https://doi.org/10.5194/acp-16-4987-2016>
- Canagaratna, M. R., Jimenez, J. L., Kroll, J. H., Chen, Q., Kessler, S. H., Massoli, P., et al. (2015). Elemental ratio measurements of organic compounds using aerosol mass spectrometry: Characterization, improved calibration, and implications. *Atmospheric Chemistry and Physics*, *15*(1), 253–297. <https://doi.org/10.5194/acp-15-253-2015>
- Capes, G., Johnson, B., McFiggans, G., Williams, P., Haywood, J., & Coe, H. (2008). Aging of biomass burning aerosols over West Africa: Aircraft measurements of chemical composition, microphysical properties, and emission ratios. *Journal of Geophysical Research*, *113*, D00C15. <https://doi.org/10.1029/2008JD009845>
- Chacon-Madrid, H., & Donahue, N. (2011). Fragmentation vs. functionalization: Chemical aging and organic aerosol formation. *Atmospheric Chemistry and Physics*, *11*, 10,553–10,563. <https://doi.org/10.5194/acp-11-10553-2011>

- Chen, Q., Liu, Y., Donahue, N. M., Shilling, J. E., & Martin, S. T. (2011). Particle-phase chemistry of secondary organic material: Modeled compared to measured O:C and H:C elemental ratios provide constraints. *Environmental Science & Technology*, *45*(11), 4763–4770. <https://doi.org/10.1021/es104398s>
- Chylek, P., Lee, J. E., Romonosky, D. E., Gallo, F., Lou, S., Shrivastava, M., et al. (2019). Mie scattering captures observed optical properties of ambient biomass burning plumes assuming uniform black, brown, and organic carbon mixtures. *Journal of Geophysical Research: Atmosphere*, *124*, 11,406–11,427. <https://doi.org/10.1029/2019JD031224>
- Claeys, M., Graham, B., Vas, G., Wang, W., Vermeylen, R., Pashynska, V., et al. (2004). Formation of secondary organic aerosols through photooxidation of isoprene. *Science*, *303*(5661), 1173–1176. <https://doi.org/10.1126/science.1092805>
- Collier, S., Williams, L. R., Onasch, T. B., Cappa, C. D., Zhang, X., Russell, L. M., et al. (2018). Influence of emissions and aqueous processing on particles containing black carbon in a polluted urban environment: Insights from a soot particle—Aerosol mass spectrometer. *Journal of Geophysical Research: Atmospheres*, *123*, 6648–6666. <https://doi.org/10.1002/2017JD027851>
- Cubison, M., Ortega, A., Hayes, P., Farmer, D., Day, D., Lechner, M., et al. (2011). Effects of aging on organic aerosol from open biomass burning smoke in aircraft and laboratory studies. *Atmospheric Chemistry and Physics*, *11*(23), 12,049–12,064. <https://doi.org/10.5194/acp-11-12049-2011>
- Dentener, F., Kinne, S., Bond, T., Boucher, O., Cofala, J., Generoso, S., et al. (2006). Emissions of primary aerosol and precursor gases in the years 2000 and 1750 prescribed data-sets for AeroCom. *Atmospheric Chemistry and Physics*, *6*(12), 4321–4344. <https://doi.org/10.5194/acp-6-4321-2006>
- Dunlea, E. J., DeCarlo, P. F., Aiken, A. C., Kimmel, J. R., Peltier, R. E., Weber, R. J., et al. (2009). Evolution of Asian aerosols during transpacific transport in INTEX-B. *Atmospheric Chemistry and Physics*, *9*(19), 7257–7287. <https://doi.org/10.5194/acp-9-7257-2009>
- Epstein, S. A., Blair, S. L., & Nizkorodov, S. A. (2014). Direct photolysis of α -pinene ozonolysis secondary organic aerosol: Effect on particle mass and peroxide content. *Environmental Science & Technology*, *48*(19), 11,251–11,258. <https://doi.org/10.1021/es502350u>
- Forrister, H., Liu, J., Scheuer, E., Dibb, J., Ziemba, L., Thornhill, K. L., et al. (2015). Evolution of brown carbon in wildfire plumes. *Geophysical Research Letters*, *42*, 4623–4630. <https://doi.org/10.1002/2015GL063897>
- Garofalo, L. A., Pothier, M. A., Levin, E. J., Campos, T., Kreidenweis, S. M., & Farmer, D. K. (2019). Emission and evolution of submicron organic aerosol in smoke from wildfires in the western United States. *ACS Earth and Space Chemistry*, *3*(7), 1237–1247. <https://doi.org/10.1021/acsearthspacechem.9b00125>
- Glasius, M., & Goldstein, A. H. (2016). Recent discoveries and future challenges in atmospheric organic chemistry. *Environmental Science & Technology*, *50*(6), 2754–2764. <https://doi.org/10.1021/acs.est.5b05105>
- Glotfelty, T., He, J., & Zhang, Y. (2017). Improving organic aerosol treatments in CESM/CAM5: Development, application, and evaluation. *Journal of Advances in Modeling Earth Systems*, *9*, 1506–1539. <https://doi.org/10.1002/2016MS000874>
- Guenther, A., Karl, T., Harley, P., Wiedinmyer, C., Palmer, P. I., & Geron, C. (2006). Estimates of global terrestrial isoprene emissions using MEGAN (Model of Emissions of Gases and Aerosols from Nature). *Atmospheric Chemistry and Physics*, *6*, 3181–3210. <https://doi.org/10.5194/acp-6-3181-2006>
- Guenther, A. B., Jiang, X., Heald, C. L., Sakulyanontvittaya, T., Duhl, T., Emmons, L. K., & Wang, X. (2012). The Model of Emissions of Gases and Aerosols from Nature Version 2.1 (MEGAN2.1): An extended and updated framework for modeling biogenic emissions. *Geoscientific Model Development*, *5*, 1471–1492. <https://doi.org/10.5194/gmd-5-1471-2012>
- Hallquist, M., Wenger, J. C., Baltensperger, U., Rudich, Y., Simpson, D., Claeys, M., et al. (2009). The formation, properties and impact of secondary organic aerosol: Current and emerging issues. *Atmosphere Chemistry Physics*, *9*(14), 5155–5236. <https://doi.org/10.5194/acp-9-5155-2009>
- Heald, C., Coe, H., Jimenez, J., Weber, R., Bahreini, R., Middlebrook, A., et al. (2011). Exploring the vertical profile of atmospheric organic aerosol: Comparing 17 aircraft field campaigns with a global model. *Atmospheric Chemistry and Physics*, *11*(24), 12,673–12,696. <https://doi.org/10.5194/acp-11-12673-2011>
- Heald, C., Ridley, D., Kroll, J., Barrett, S., Cady-Pereira, K., Alvarado, M., & Holmes, C. (2014). Contrasting the direct radiative effect and direct radiative forcing of aerosols. *Atmospheric Chemistry and Physics*, *14*, 5513–5527. <https://doi.org/10.5194/acp-14-5513-2014>
- Heald, C. L., Ridley, D. A., Kreidenweis, S. M., & Drury, E. E. (2010). Satellite observations cap the atmospheric organic aerosol budget. *Geophysical Research Letters*, *37*, L24808. <https://doi.org/10.1029/2010GL045095>
- Henry, K. M., & Donahue, N. M. (2012). Photochemical aging of α -pinene secondary organic aerosol: Effects of OH radical sources and photolysis. *The Journal of Physical Chemistry A*, *116*(24), 5932–5940. <https://doi.org/10.1021/jp210288s>
- Hermansson, E., Roldin, P., Rusanen, A., Mogensen, D., Kivekäs, N., Väänänen, R., et al. (2014). Biogenic SOA formation through gas-phase oxidation and gas-to-particle partitioning—A comparison between process models of varying complexity. *Atmospheric Chemistry and Physics*, *14*(21), 11,853–11,869. <https://doi.org/10.5194/acp-14-11853-2014>
- Hess, M., Koepke, P., & Schult, I. (1998). Optical properties of aerosols and clouds: The software package OPAC. *Bulletin of the American Meteorological Society*, *79*(5), 831–844.
- Hodshire, A. L., Akherati, A., Alvarado, M. J., Brown-Steiner, B., Jathar, S. H., Jimenez, J. L., et al. (2019). Aging effects on biomass burning aerosol mass and composition: A critical review of field and laboratory studies. *Environmental Science & Technology*, *53*(17), 10,007–10,022. <https://doi.org/10.1021/acs.est.9b02588>
- Hodshire, A. L., Bian, Q., Ramnarine, E., Lonsdale, C. R., Alvarado, M. J., Kreidenweis, S. M., et al. (2019). More than emissions and chemistry: Fire size, dilution, and background aerosol also greatly influence near-field biomass burning aerosol aging. *Journal of Geophysical Research: Atmospheres*, *124*, 5589–5611. <https://doi.org/10.1029/2018JD029674>
- Hodzic, A., Campuzano-Jost, P., Bian, H., Chin, M., Colarco, P. R., Day, D. A., et al. (2020). Characterization of organic aerosol across the global remote troposphere: A comparison of ATom measurements and global chemistry models. *Atmospheric Chemistry and Physics*, *20*(8), 4607–4635. <https://doi.org/10.5194/acp-20-4607-2020>
- Hodzic, A., Kasibhatla, P. S., Jo, D. S., Cappa, C. D., Jimenez, J. L., Madronich, S., & Park, R. J. (2016). Rethinking the global secondary organic aerosol (SOA) budget: Stronger production, faster removal, shorter lifetime. *Atmospheric Chemistry and Physics*, *16*, 7917–7941. <https://doi.org/10.5194/acp-16-7917-2016>
- Hodzic, A., Madronich, S., Kasibhatla, P., Tyndall, G., Aumont, B., Jimenez, J., et al. (2015). Organic photolysis reactions in tropospheric aerosols: Effect on secondary organic aerosol formation and lifetime. *Atmospheric Chemistry and Physics*, *15*(16), 9253–9269. <https://doi.org/10.5194/acp-15-9253-2015>
- Hoesly, R. M., Smith, S. J., Feng, L., Klimont, Z., Janssens-Maenhout, G., Pitkanen, T., et al. (2018). Historical (1750–2014) anthropogenic emissions of reactive gases and aerosols from the Community Emissions Data System (CEDs). *Geoscientific Model Development*, *11*(1), 369–408. <https://doi.org/10.5194/gmd-11-369-2018>

- Hu, J., Huang, L., Chen, M., Liao, H., Zhang, H., Wang, S., et al. (2017). Premature mortality attributable to particulate matter in China: Source contributions and responses to reductions. *Environmental Science & Technology*, *51*(17), 9950–9959. <https://doi.org/10.1021/acs.est.7b03193>
- Hu, W., Palm, B. B., Day, D. A., Campuzano-Jost, P., Krechmer, J. E., Peng, Z., et al. (2016). Volatility and lifetime against OH heterogeneous reaction of ambient isoprene-epoxydiols-derived secondary organic aerosol (IEPOX-SOA). *Atmospheric Chemistry and Physics*, *16*(18), 11,563–11,580. <https://doi.org/10.5194/acp-16-11563-2016>
- Hu, W. W., Campuzano-Jost, P., Palm, B. B., Day, D. A., Ortega, A. M., Hayes, P. L., et al. (2015). Characterization of a real-time tracer for isoprene epoxydiols-derived secondary organic aerosol (IEPOX-SOA) from aerosol mass spectrometer measurements. *Atmospheric Chemistry and Physics*, *15*(20), 11,807–11,833. <https://doi.org/10.5194/acp-15-11807-2015>
- Hunter, J. F., Day, D. A., Palm, B. B., Yataavelli, R. L. N., Chan, A. W. H., Kaser, L., et al. (2017). Comprehensive characterization of atmospheric organic carbon at a forested site. *Nature Geoscience*, *10*(10), 748–753. <https://doi.org/10.1038/NGEO3018>
- Jacob, D. J., Crawford, J., Maring, H., Clarke, A., Dibb, J. E., Emmons, L., et al. (2010). The Arctic Research of the Composition of the Troposphere from Aircraft and Satellites (ARCTAS) mission: Design, execution, and first results. *Atmospheric Chemistry and Physics*, *10*(11), 5191–5212. <https://doi.org/10.5194/acp-10-5191-2010>
- Jimenez, J. L., Canagaratna, M. R., Donahue, N. M., Prevot, A. S. H., Zhang, Q., Kroll, J. H., et al. (2009). Evolution of organic aerosols in the atmosphere. *Science*, *326*(5959), 1525–1529. <https://doi.org/10.1126/science.1180353>
- Jokinen, T., Berndt, T., Makkonen, R., Kerminen, V. M., Junninen, H., Paasonen, P., et al. (2015). Production of extremely low volatile organic compounds from biogenic emissions: Measured yields and atmospheric implications. *Proceedings of the National Academy of Sciences*, *112*(23), 7123–7128. <https://www.pnas.org/content/112/23/7123>, <https://doi.org/10.1073/pnas.1423977112>
- Jolleys, M. D., Coe, H., McFiggans, G., Capes, G., Allan, J. D., Crosier, J., et al. (2012). Characterizing the aging of biomass burning organic aerosol by use of mixing ratios: A meta-analysis of four regions. *Environmental Science & Technology*, *46*(24), 13,093–13,102. <https://doi.org/10.1021/es302386v>
- Kaiser, J., Heil, A., Andreae, M., Benedetti, A., Chubarova, N., Jones, L., et al. (2012). Biomass burning emissions estimated with a global fire assimilation system based on observed fire radiative power. *Biogeosciences*, *9*(1), 527–554. <https://doi.org/10.5194/bg-9-527-2012>
- Kalberer, M., Paulsen, D., Sax, M., Steinbacher, M., Dommen, J., Prevot, A. S. H., et al. (2004). Identification of polymers as major components of atmospheric organic aerosols. *Science*, *303*(5664), 1659–1662. <https://doi.org/10.1126/science.1092185>
- Kanakidou, M., Seinfeld, J. H., Pandis, S. N., Barnes, I., Dentener, F. J., Facchini, M. C., et al. (2005). Organic aerosol and global climate modelling: a review. *Atmospheric Chemistry and Physics*, *5*, 1053–1123. <https://doi.org/10.5194/acp-5-1053-2005>
- Kelly, J. M., Doherty, R. M., O'Connor, F. M., & Mann, G. W. (2018). The impact of biogenic, anthropogenic, and biomass burning volatile organic compound emissions on regional and seasonal variations in secondary organic aerosol. *Atmospheric Chemistry and Physics*, *18*, 7393–7422. <https://doi.org/10.5194/acp-18-7393-2018>
- Kim, P. S., Jacob, D. J., Fisher, J. A., Travis, K., Yu, K., Zhu, L., et al. (2015). Sources, seasonality, and trends of southeast US aerosol: An integrated analysis of surface, aircraft, and satellite observations with the GEOS-Chem chemical transport model. *Atmospheric Chemistry and Physics*, *15*(18), 10,411–10,433. <https://doi.org/10.5194/acp-15-10411-2015>
- Kleindienst, T. E., Lewandowski, M., Offenberg, J. H., Jaoui, M., & Edney, E. O. (2007). Ozone-isoprene reaction: Re-examination of the formation of secondary organic aerosol. *Geophysical Research Letters*, *34*, L01805. <https://doi.org/10.1029/2006GL027485>
- Kroll, J. H., Donahue, N. M., Jimenez, J. L., Kessler, S. H., Canagaratna, M. R., Wilson, K. R., et al. (2011). Carbon oxidation state as a metric for describing the chemistry of atmospheric organic aerosol. *Nature Chemistry*, *3*(2), 133–139. <https://doi.org/10.1038/nchem.948>
- Kroll, J. H., & Seinfeld, J. H. (2008). Chemistry of secondary organic aerosol: Formation and evolution of low-volatility organics in the atmosphere. *Atmospheric Environment*, *42*(16), 3593–3624. <https://doi.org/10.1016/j.atmosenv.2008.01.003>
- Lamarque, J.-F., Emmons, L. K., Hess, P. G., Kinnison, D. E., Tilmes, S., Vitt, F., et al. (2012). CAM-chem: Description and evaluation of interactive atmospheric chemistry in the Community Earth System Model. *Geoscientific Model Development*, *5*(2), 369–411. <https://doi.org/10.5194/gmd-5-369-2012>
- Lambe, A. T., Onasch, T. B., Croasdale, D. R., Wright, J. P., Martin, A. T., Franklin, J. P., et al. (2012). Transitions from functionalization to fragmentation reactions of laboratory secondary organic aerosol (SOA) generated from the OH oxidation of alkane precursors. *Environmental Science & Technology*, *46*(10), 5430–5437. <https://doi.org/10.1021/es300274t>
- Lathière, J., Hauglustaine, D. A., De Noblet-Ducoudre, N., Krinner, G., & Folberth, G. A. (2005). Past and future changes in biogenic volatile organic compound emissions simulated with a global dynamic vegetation model. *Geophysical Research Letters*, *32*, L20818. <https://doi.org/10.1029/2005GL024164>
- Lee, J. E., Dubey, M. K., Aiken, A. C., Chylek, P., & Carrico, C. M. (2020). Optical and chemical analysis of absorption enhancement by mixed carbonaceous aerosols in the 2019 Woodbury, AZ fire plume. *Journal of Geophysical Research: Atmospheres*, *25*, e2020JD032399. <https://doi.org/10.1029/2020JD032399>
- Levy, R., & Hsu, C. (2015). *Modis atmosphere l2 aerosol product, NASA MODIS adaptive processing system*. USA: Goddard Space Flight Center.
- Liu, X., Easter, R. C., Ghan, S. J., Zaveri, R., Rasch, P., Shi, X., et al. (2012). Toward a minimal representation of aerosols in climate models: Description and evaluation in the Community Atmosphere Model CAM5. *Geoscientific Model Development*, *5*(3), 709–739. <https://doi.org/10.5194/gmd-5-709-2012>
- Liu, J. C., Mickley, L. J., Sulprizio, M. P., Dominici, F., Yue, X., Ebisu, K., et al. (2016). Particulate air pollution from wildfires in the western US under climate change. *Climatic Change*, *138*(3), 655–666. <https://doi.org/10.1007/s10584-016-1762-6>
- Liu, X., Ma, P.-L., Wang, H., Tilmes, S., Singh, B., Easter, R., et al. (2016). Description and evaluation of a new four-mode version of the Modal Aerosol Module (MAM4) within Version 5.3 of the Community Atmosphere Model. *Geoscientific Model Development*, *9*(2), 505–522. <https://doi.org/10.5194/gmd-9-505-2016>
- Liu, X., Zhang, Y., Huey, L. G., Yokelson, R. J., Wang, Y., Jimenez, J. L., et al. (2016). Agricultural fires in the southeastern U.S. during SEAC4RS: Emissions of trace gases and particles and evolution of ozone, reactive nitrogen, and organic aerosol. *Journal of Geophysical Research: Atmospheres*, *99*, 1347–1370. <https://doi.org/10.1029/93JD02916>
- Malecha, K. T., Cai, Z., & Nizkorodov, S. A. (2018). Photodegradation of secondary organic aerosol material quantified with a quartz crystal microbalance. *Environmental Science & Technology Letters*, *5*(6), 366–371. <https://doi.org/10.1021/acs.estlett.8b00231>
- Malm, W. C., Sisler, J. F., Huffman, D., Eldred, R. A., & Cahill, T. A. (1994). Spatial and seasonal trends in particle concentration and optical extinction in the United States. *Journal of Geophysical Research*, *99*(D1), 1347–1370. <https://doi.org/10.1029/93JD02916>
- Martin, S., Artaxo, P., Machado, L., Manzi, A., Souza, R., Schumacher, C., et al. (2016). Introduction: Observations and modeling of the green ocean Amazon (GoAmazon2014/5). *Atmospheric Chemistry and Physics*, *16*, 4785–4797. <https://doi.org/10.5194/acp-16-4785-2016>

- Mei, F., Wang, J., Comstock, J. M., Weigel, R., Krämer, M., Mahnke, C., et al. (2020). Comparison of aircraft measurements during GoAmazon2014/5 and ACRIDICON-CHUVA. *Atmospheric Measurement Techniques*, *13*(2), 661–684. <https://doi.org/10.5194/amt-13-661-2020>
- Ming, Y., Ramaswamy, V., Ginoux, P. A., & Horowitz, L. H. (2005). Direct radiative forcing of anthropogenic organic aerosol. *Journal of Geophysical Research*, *110*, D20208. <https://doi.org/10.1029/2004JD005573>
- Murphy, B., Donahue, N. M., Fountoukis, C., Dall'Osto, M., O'dowd, C., Kiendler-Scharr, A., & Pandis, S. N. (2012). Functionalization and fragmentation during ambient organic aerosol aging: Application of the 2-D volatility basis set to field studies. *Atmospheric Chemistry and Physics*, *12*, 10,797–10,816. <https://doi.org/10.5194/acp-12-10797-2012>
- Myhre, G., Berglen, T. F., Johnsrud, M., Hoyle, C., Bernsten, T. K., Christopher, S., et al. (2009). Modelled radiative forcing of the direct aerosol effect with multi-observation evaluation. *Atmospheric Chemistry and Physics*, *9*(4), 1365–1392. <https://doi.org/10.5194/acp-9-1365-2009>
- Myhre, G., Samset, B. H., Schulz, M., Balkanski, Y., Bauer, S., Bernsten, T. K., et al. (2013). Radiative forcing of the direct aerosol effect from AeroCom Phase II simulations. *Atmospheric Chemistry and Physics*, *13*(4), 1853–1877. <https://doi.org/10.5194/acp-13-1853-2013>
- Ng, N. L., Chhabra, P. S., Chan, A. W. H., Surratt, J. D., Kroll, J. H., Kwan, A. J., et al. (2007). Effect of NO_x level on secondary organic aerosol (SOA) formation from the photooxidation of terpenes. *Atmospheric Chemistry and Physics*, *7*(19), 5159–5174. <https://doi.org/10.5194/acp-7-5159-2007>
- Ng, N. L., Kwan, A. J., Surratt, J. D., Chan, A. W. H., Chhabra, P. S., Sorooshian, A., et al. (2008). Secondary organic aerosol (SOA) formation from reaction of isoprene with nitrate radicals (NO₃). *Atmospheric Chemistry and Physics*, *8*(14), 4117–4140. <https://doi.org/10.5194/acp-8-4117-2008>
- O'Brien, R. E., & Kroll, J. H. (2019). Photolytic aging of secondary organic aerosol: Evidence for a substantial photo-recalcitrant fraction. *The journal of physical chemistry letters*, *10*(14), 4003–4009. <https://doi.org/10.1021/acs.jpclett.9b01417>
- Pistone, K., Redemann, J., Doherty, S., Zuidema, P., Burton, S., Cairns, B., et al. (2019). Intercomparison of biomass burning aerosol optical properties from in situ and remote-sensing instruments in ORACLES-2016. *Atmospheric Chemistry and Physics*, *19*(14), 9181–9208. <https://doi.org/10.5194/acp-19-9181-2019>
- Ranjithkumar, A., Gordon, H., Williamson, C., Rollins, A., Pringle, K. J., Kupc, A. et al. (2020). Constraints on global aerosol number concentration, SO₂ and condensation sink in UKESM1 using ATom measurements, *Atmospheric Chemistry and Physics Discussions*, <https://doi.org/10.5194/acp-2020-1071>, in review.
- Rasch, P. J., Xie, S., Ma, P.-L., Lin, W., Wang, H., Tang, Q., et al. (2019). An overview of the atmospheric component of the Energy Exascale Earth System Model. *Journal of Advances in Modeling Earth Systems*, *11*, 2377–2411. <https://doi.org/10.1029/2019MS001629>
- Reddington, C. L., Morgan, W. T., Darbyshire, E., Brito, J., Coe, H., Artaxo, P., et al. (2019). Biomass burning aerosol over the Amazon: Analysis of aircraft, surface and satellite observations using a global aerosol model. *Atmospheric Chemistry and Physics*, *19*(14), 9125–9152. <https://doi.org/10.5194/acp-19-9125-2019>
- Reddington, C. L., Spracklen, D. V., Artaxo, P., Ridley, D. A., Rizzo, L. V., & Arana, A. (2016). Analysis of particulate emissions from tropical biomass burning using a global aerosol model and long-term surface observations. *Atmospheric Chemistry and Physics*, *16*, 11,083–11,106. <https://doi.org/10.5194/acp-16-11083-2016>
- Reid, J. S., Koppmann, R., Eck, T. F., & Eleuterio, D. P. (2005). A review of biomass burning emissions part II: intensive physical properties of biomass burning particles. *Atmospheric Chemistry and Physics*, *5*(3), 799–825. <https://doi.org/10.5194/acp-5-799-2005>
- Ridley, D., Heald, C., Ridley, K., & Kroll, J. (2018). Causes and consequences of decreasing atmospheric organic aerosol in the United States. *Proceedings of the National Academy of Sciences*, *115*(2), 290–295. <https://doi.org/10.1073/pnas.1700387115>
- Robinson, A. L., Donahue, N. M., Shrivastava, M. K., Weitkamp, E. A., Sage, A. M., Grieshop, A. P., et al. (2007). Rethinking organic aerosols: Semivolatile emissions and photochemical aging. *Science*, *315*(5816), 1259–1262. <https://doi.org/10.1126/science.113306>
- Sakaeda, N., Wood, R., & Rasch, P. J. (2011). Direct and semidirect aerosol effects of southern African biomass burning aerosol. *Journal of Geophysical Research*, *116*, D12205. <https://doi.org/10.1029/2010JD015540>
- Schroder, J. C., Campuzano-Jost, P., Day, D. A., Shah, V., Larson, K., Sommers, J. M., et al. (2018). Sources and secondary production of organic aerosols in the Northeastern United States during WINTER. *Journal of Geophysical Research: Atmospheres*, *123*(14), 7771–7796. <https://doi.org/10.1029/2018JD028475>
- Schulz, C., Schneider, J., Holanda, B. A., Appel, O., Costa, A., de Sá, S. S., et al. (2018). Aircraft-based observations of isoprene-epoxydiol-derived secondary organic aerosol (IEPOX_SOA) in the tropical upper troposphere over the Amazon region. *Atmospheric Chemistry and Physics*, *18*(20), 14,979–15,001. <https://doi.org/10.5194/acp-18-14979-2018>
- Schulz, M., Textor, C., Kinne, S., Balkanski, Y., Bauer, S., Bernsten, T., et al. (2006). Radiative forcing by aerosols as derived from the AeroCom present-day and pre-industrial simulations. *Atmospheric Chemistry and Physics*, *6*(12), 5225–5246. <https://doi.org/10.5194/acp-6-5225-2006>
- Sengupta, K., Pringle, K., Johnson, J. S., Reddington, C., Browse, J., Scott, C. E., & Carslaw, K. (2020). A global model perturbed parameter ensemble study of secondary organic aerosol formation. *Atmospheric Chemistry and Physics Discussions*. <https://doi.org/10.5194/acp-2020-756>
- Shah, V., Jaegle, L., Jimenez, J. L., Schroder, J. C., Campuzano-Jost, P., Campos, T. L., et al. (2019). Widespread pollution from secondary sources of organic aerosols during winter in the northeastern United States. *Geophysical Research Letters*, *46*, 2974–2983. <https://doi.org/10.1029/2018GL081530>
- Shilling, J. E., Chen, Q., King, S. M., Rosenoern, T., Kroll, J. H., Worsnop, D. R., et al. (2009). Loading-dependent elemental composition of α -pinene SOA particles. *Atmospheric Chemistry and Physics*, *9*(3), 771–782. <https://doi.org/10.5194/acp-9-771-2009>
- Shilling, J. E., Chen, Q., King, S. M., Rosenoern, T., Kroll, J. H., Worsnop, D. R., et al. (2008). Particle mass yield in secondary organic aerosol formed by the dark ozonolysis of alpha-pinene. *Atmospheric Chemistry and Physics*, *8*(7), 2073–2088. <https://doi.org/10.5194/acp-8-2073-2008>
- Shilling, J. E., Pekour, M. S., Fortner, E. C., Artaxo, P., de Sá, S., Hubbe, J. M., et al. (2018). Aircraft observations of the chemical composition and aging of aerosol in the Manaus urban plume during GoAmazon 2014/5. *Atmospheric Chemistry and Physics*, *18*(14), 10,773–10,797. <https://doi.org/10.5194/acp-18-10773-2018>
- Shrivastava, M., Andreae, M. O., Artaxo, P., Barbosa, H. M., Berg, L. K., Brito, J., et al. (2019). Urban pollution greatly enhances formation of natural aerosols over the Amazon rainforest. *Nature Communications*, *10*(1), 1046. <https://doi.org/10.1038/s41467-019-08909-4>
- Shrivastava, M., Cappa, C. D., Fan, J., Goldstein, A. H., Guenther, A. B., Jimenez, J. L., et al. (2017). Recent advances in understanding secondary organic aerosol: Implications for global climate forcing. *Reviews of Geophysics*, *55*, 509–559. <https://doi.org/10.1002/2016RG000540>

- Shrivastava, M., Easter, R. C., Liu, X., Zelenyuk, A., Singh, B., Zhang, K., et al. (2015). Global transformation and fate of SOA: Implications of low-volatility SOA and gas-phase fragmentation reactions. *Journal of Geophysical Research: Atmospheres*, *120*, 4169–4195. <https://doi.org/10.1002/2014JD022563>
- Shrivastava, M., Zelenyuk, A., Imre, D., Easter, R., Beranek, J., Zaveri, R. A., & Fast, J. (2013). Implications of low volatility SOA and gas-phase fragmentation reactions on SOA loadings and their spatial and temporal evolution in the atmosphere. *Journal of Geophysical Research: Atmospheres*, *118*, 3328–3342. <https://doi.org/10.1002/jgrd.50160>
- Sindelarova, K., Granier, C., Bouarar, I., Guenther, A., Tilmes, S., Stavrou, T., et al. (2014). Global data set of biogenic VOC emissions calculated by the MEGAN model over the last 30 years. *Atmospheric Chemistry and Physics*, *14*(17), 9317–9341. <https://doi.org/10.5194/acp-14-9317-2014>
- Slade, J. H., Shiraiwa, M., Arangio, A., Su, H., Pöschl, U., Wang, J., & Knopf, D. A. (2017). Cloud droplet activation through oxidation of organic aerosol influenced by temperature and particle phase state. *Geophysical Research Letters*, *44*, 1583–1591. <https://doi.org/10.1002/2016GL072424>
- Sporre, M. K., Blichner, S. M., Schrödner, R., Karset, I. H. H., Berntsen, T. K., van Noije, T., et al. (2020). Large difference in aerosol radiative effects from BVOC-SOA treatment in three Earth system models. *Atmospheric Chemistry and Physics*, *20*(14), 8953–8973. <https://doi.org/10.5194/acp-20-8953-2020>
- Spracklen, D., Jimenez, J., Carslaw, K., Worsnop, D., Evans, M., Mann, G., et al. (2011). Aerosol mass spectrometer constraint on the global secondary organic aerosol budget. *Atmospheric Chemistry and Physics*, *11*(23), 12,109–12,136. <https://doi.org/10.5194/acp-11-12109-2011>
- Sun, J., Zhang, K., Wan, H., Ma, P.-L., Tang, Q., & Zhang, S. (2019). Impact of nudging strategy on the climate representativeness and hindcast skill of constrained EAMv1 simulations. *Journal of Advances in Modeling Earth Systems*, *11*, 3911–3933. <https://doi.org/10.1029/2019MS001831>
- Tilmes, S., Hodzic, A., Emmons, L. K., Mills, M. J., Gettelman, A., Kinnison, D. E., et al. (2019). Climate forcing and trends of organic aerosols in the Community Earth System Model (CESM2). *Journal of Advances in Modeling Earth Systems*, *11*, 4323–4351. <https://doi.org/10.1029/2019MS001827>
- Tosca, M., Randerson, J., & Zender, C. (2013). Global impact of smoke aerosols from landscape fires on climate and the Hadley circulation. *Atmospheric Chemistry and Physics*, *13*, 5227–5241. <https://doi.org/10.5194/acp-13-5227-2013>
- Tsigaridis, K., Daskalakis, N., Kanakidou, M., Adams, P., Artaxo, P., Bahadur, R., et al. (2014). The AeroCom evaluation and intercomparison of organic aerosol in global models. *Atmospheric Chemistry and Physics*, *14*(19), 10,845–10,895. <https://doi.org/10.5194/acp-14-10845-2014>
- Tsigaridis, K., & Kanakidou, M. (2018). The present and future of secondary organic aerosol direct forcing on climate. *Current Climate Change Reports*, *4*(2), 84–98. <https://doi.org/10.1007/s40641-018-0092-3>
- Turpin, B. J., & Lim, H.-J. (2001). Species contributions to PM_{2.5} mass concentrations: Revisiting common assumptions for estimating organic mass. *Aerosol Science & Technology*, *35*(1), 602–610. <https://doi.org/10.1080/02786820119445>
- Vakkari, V., Beukes, J. P., Maso, M. D., Aurela, M., Josipovic, M., & van Zyl, P. G. (2018). Major secondary aerosol formation in southern African open biomass burning plumes. *Nature Geoscience*, *11*(8), 580–583. <https://doi.org/10.1038/s41561-018-0170-0>
- van Marle, M., Kloster, S., Magi, B., Marlon, J., Daniiau, A., Field, R., et al. (2017). Historic global biomass burning emissions for CMIP6 (BB4CMIP) based on merging satellite observations with proxies and fire models (1750–2015). *Geoscientific Model Development*, *10*(9), 3329–3357. <https://doi.org/10.5194/gmd-10-3329-2017>
- Wang, H., Easter, R. C., Rasch, P. J., Wang, M., Liu, X., Ghan, S. J., et al. (2013). Sensitivity of remote aerosol distributions to representation of cloud–aerosol interactions in a global climate model. *Geoscientific Model Development*, *6*(3), 765–782. <https://doi.org/10.5194/gmd-6-765-2013>
- Wang, H., Easter, R. C., Zhang, R., Ma, P.-L., Singh, B., Zhang, K., et al. (2020). Aerosols in the E3SM Version 1: New developments and their impacts on radiative forcing. *Journal of Advances in Modeling Earth Systems*, *12*, e2019MS001851. <https://doi.org/10.1029/2019MS001851>
- Warneke, C., Froyd, K., Brioude, J., Bahreini, R., Brock, C., Cozic, J., et al. (2010). An important contribution to springtime Arctic aerosol from biomass burning in Russia. *Geophysical Research Letters*, *37*, L01801. <https://doi.org/10.1029/2009GL041816>
- Wendisch, M., Pöschl, U., Andreae, M. O., Machado, L. A., Albrecht, R., Schlager, H., et al. (2016). ACRIDICON-CHUVA campaign: Studying tropical deep convective clouds and precipitation over Amazonia using the new German research aircraft HALO. *Bulletin of the American Meteorological Society*, *97*(10), 1885–1908. <https://doi.org/10.1175/BAMS-D-14-00255.1>
- Wong, J. P., Zhou, S., & Abbatt, J. P. (2014). Changes in secondary organic aerosol composition and mass due to photolysis: Relative humidity dependence. *The Journal of Physical Chemistry A*, *119*(19), 4309–4316. <https://doi.org/10.1021/jp506898c>
- Xie, S., Lin, W., Rasch, P. J., Ma, P.-L., Neale, R., Larson, V. E., et al. (2018). Understanding cloud and convective characteristics in Version 1 of the E3SM atmosphere model. *Journal of Advances in Modeling Earth Systems*, *10*, 2618–2644. <https://doi.org/10.1029/2018MS001350>
- Yahya, K., Glotfelty, T., Wang, K., Zhang, Y., & Nenes, A. (2017). Modeling regional air quality and climate: Improving organic aerosol and aerosol activation processes in WRF/Chem Version 3.7. 1. *Geoscientific Model Development*, *10*(2333), 2333–2363. <https://doi.org/10.5194/gmd-10-2333-2017>
- Yokelson, R. J., Burling, I. R., Gilman, J. B., Warneke, C., Stockwell, C. E., Gouw, J. D., et al. (2013). Coupling field and laboratory measurements to estimate the emission factors of identified and unidentified trace gases for prescribed fires. *Atmospheric Chemistry and Physics*, *13*(1), 89–116. <https://doi.org/10.5194/acp-13-89-2013>
- Yu, P., Froyd, K. D., Portmann, R. W., Toon, O. B., Freitas, S. R., Bardeen, C. G., et al. (2019). Efficient in-cloud removal of aerosols by deep convection. *Geophysical Research Letters*, *46*, 1061–1069. <https://doi.org/10.1029/2018GL080544>
- Yu, P., Toon, O. B., Bardeen, C. G., Zhu, Y., Rosenlof, K. H., Portmann, R. W., et al. (2019). Black carbon lofts wildfire smoke high into the stratosphere to form a persistent plume. *Science*, *365*(6453), 587–590. <https://doi.org/10.1126/science.aax1748>
- Zaveri, R. A., Easter, R. C., Fast, J. D., & Peters, L. K. (2008). Model for simulating aerosol interactions and chemistry (MOSAIC). *Journal of Geophysical Research*, *113*, D13204. <https://doi.org/10.1029/2007JD008782>
- Zawadowicz, M. A., Lee, B. H., Shrivastava, M., Zelenyuk-Imre, A., Zaveri, R. A., Flynn, C., et al. (2020). Photolysis controls atmospheric budgets of biogenic secondary organic aerosol. *Environmental Science & Technology*, *54*(7), 3861–3870. <https://doi.org/10.1021/acs.est.9b07051>
- Zhang, K., Wan, H., Liu, X., Ghan, S. J., Kooperman, G. J., Ma, P.-L., et al. (2014). Technical note: On the use of nudging for aerosol–climate model intercomparison studies. *Atmospheric Chemistry and Physics*, *14*(16), 8631–8645. <https://doi.org/10.5194/acp-14-8631-2014>
- Zhang, Q., Jimenez, J. L., Canagaratna, M., Allan, J., Coe, H., Ulbrich, I., et al. (2007). Ubiquity and dominance of oxygenated species in organic aerosols in anthropogenically-influenced Northern Hemisphere midlatitudes. *Geophysical Research Letters*, *34*, L13801. <https://doi.org/10.1029/2007GL029979>

- Zhang, Q., Worsnop, D., Canagaratna, M., & Jimenez, J. L. (2005). Hydrocarbon-like and oxygenated organic aerosols in Pittsburgh: Insights into sources and processes of organic aerosols. *Atmospheric Chemistry and Physics*, 5, 3289–3311. <https://doi.org/10.5194/acp-5-3289-2005>
- Zhang, Y., Liao, H., Ding, X., Jo, D., & Li, K. (2018). Implications of RCP emissions on future concentration and direct radiative forcing of secondary organic aerosol over China. *Science of the Total Environment*, 640, 1187–1204. <https://doi.org/10.1016/j.scitotenv.2018.05.274>
- Zhao, B., Shrivastava, M., Donahue, N. M., Gordon, H., Schervish, M., Shilling, J. E., et al. (2020). High concentration of ultrafine particles in the Amazon free troposphere produced by organic new particle formation. *Proceedings of the National Academy of Sciences*, 117(41), 25,344–25,351. <https://doi.org/10.1073/pnas.2006716117>
- Zeng, L., Zhang, A., Wang, Y., Wagner, N. L., Katich, J. M., Schwarz, J. P., et al. (2020). Global measurements of brown carbon and estimated direct radiative effects. *Geophysical Research Letters*, 47(13), e2020GL088747. <https://doi.org/10.1029/2020gl088747>
- Zhou, S., Collier, S., Jaffe, D. A., Briggs, N. L., Hee, J., Sedlacek, A. J. III, et al. (2017). Regional influence of wildfires on aerosol chemistry in the western US and insights into atmospheric aging of biomass burning organic aerosol. *Atmospheric Chemistry and Physics*, 17(3), 2477–2493. <https://doi.org/10.5194/acp-17-2477-2017>
- Zhu, J., Penner, J. E., Lin, G., Zhou, C., Xu, L., & Zhuang, B. (2017). Mechanism of SOA formation determines magnitude of radiative effects. *Proceedings of the National Academy of Sciences*, 114(48), 12,685–12,690. <https://doi.org/10.1073/pnas.1712273114>
- Zhu, J., Penner, J. E., Yu, F., Sillman, S., Andreae, M. O., & Coe, H. (2019). Decrease in radiative forcing by organic aerosol nucleation, climate, and land use change. *Nature Communications*, 10(1), 423. <https://doi.org/10.1038/s41467-019-08407-7>
- Ziemann, P. J., & Atkinson, R. (2012). Kinetics, products, and mechanisms of secondary organic aerosol formation. *Chemical Society Reviews*, 41(19), 6582–6605. <https://doi.org/10.1039/c2cs35122f>